

HERA the new frontier

J.Feltesse

DAPNIA-SPP, CE-Saclay
91191 Gif-sur-Yvette Cedex, France

Lectures presented at the SLAC Summer Institute
Stanford, California, August 5 - August 16, 1991

© J. Feltesse 1992

1 Introduction

The large storage ring HERA (Hadronen-Elektronen-Ring-Anlage or Hadron-Electron-Ring-Accelerator) has been completed at DESY (Hamburg). The large detectors H1 and ZEUS should be rolled in early 1992. The first collisions for physics studies are scheduled for spring 1992. In contrast to the electron-electron or hadron-hadron colliders for which several generations exist since more than two decades, HERA is the first electron proton storage ring ever built. Electrons and protons of nominal energies $E_e = 30 \text{ GeV}$ and $E_p = 820 \text{ GeV}$ will collide head on. The centre of mass energy is:

$$s^{1/2} = (4E_e E_p)^{1/2} = 314 \text{ GeV} \quad (1)$$

This is equivalent to an electron beam of 50 TeV impinging on a fixed hydrogen target. The beam energies can be varied, while keeping a sufficient luminosity, within the following limits: $E_e = 10\text{-}35 \text{ GeV}$ and $E_p = 300\text{-}1000 \text{ GeV}$.

The design luminosity is $1.5 \cdot 10^{31} \text{ cm}^{-2} \text{ s}^{-1}$. The total luminosity accumulated per year and per experiment could thus reach 100 pb^{-1} . HERA is also designed to produce longitudinally polarised electron or positron beams. A very detailed view of the physics expected at HERA will be provided in the proceedings of the workshop on HERA physics to be held at DESY in October 1991 [1].

This lecture will present some salient aspects of the physics potentials with a strong emphasis on the new domain offered by HERA at very small x , the momentum fraction carried by the struck quark inside the proton.

In the next section (section 2) the theoretical motivations and questions raised by Quantum Chromodynamics in this new domain will be approached at a phenomenological level. Deeper theoretical grounds on small x physics are given in the lecture of R. Peccei in these proceedings. Section (3) is devoted to the measurement of x and Q^2 in the whole accessible domain at HERA energies from the scattered electron and hadron flow laboratory variables. In section (4), the various experimental methods to extract the gluon distribution are described. Other physics opportunities to test the standard model are briefly given in section (5). Finally, section (6) is devoted to a few examples of processes not expected by the standard model but within reach at HERA.

2 Small x physics

2.1 Motivations

The x and Q^2 dependence of parton distributions at very small x ($x < 0.01$) is one of the most promising domains in QCD. In this new regime the evolution equations must go beyond the usual $LL(Q^2)$ perturbation approximations and reach the saturation region [2] [3]. Small x deep inelastic scattering probes QCD in a regime at the frontier between the well known perturbative domain and the almost unknown non perturbative domain, usually described by Regge trajectories. The small x domain at HERA is an access to the onset of non perturbative physics.

Furthermore, at the future proton proton colliders, parton distributions at small x are of utmost importance to predict signal and backgrounds of many processes, such as heavy flavors productions, jets etc. The behaviour of the parton distributions at small x is also crucial for many physical processes at present accelerators :

- Shadowing in deep inelastic scattering (EMC effect). The attenuation of the cross section on heavy nuclei at small x ($x < 0.05$) is attributed to gluon recombinations involving several nucleons [3].
- Central rapidity region of heavy ions collisions. Initial energy density depends on the square of the gluon density at small x . [4].
- Production of minijets in high energy proton collisions. Cross sections are large, in the millibarn range, but calculable, because involving hard scattering processes at virtualities of a few GeV [2,5,6].

A better understanding of the small x partons may also give some clues to approach some well known non perturbative phenomena as rising of the total cross section nucleon-nucleon or even confinement.

2.2 Kinematics

Deep inelastic scattering of leptons on nucleons is an inclusive process which depends on three variables: s , Q^2 and x . s is the square of the energy in the centre of mass. Q^2 , the square of the four-momentum transfer, defines the resolution by which the electron probes the short-distance structure of the nucleon; x , the Bjorken scaling variable, is the momentum fraction carried by the struck quark inside the nucleon. It is also sometimes convenient to use y which describes, in the rest frame of the proton, the energy transfer from the incoming to the outgoing electron. These variables are uniquely

defined in terms of l , l' and P , the four-momentum vectors of the incoming lepton, the outgoing lepton and the incoming proton respectively (Fig. 1).

$$\begin{aligned} Q^2 &= -(l - l')^2 \\ x &= Q^2/(2Pq) \\ y &= (Pq)/(Pl) \end{aligned} \quad (2)$$

where $q = l - l'$.

These variables are trivially related by

$$Q^2 = sxy \quad (3)$$

From the equations (2), it is straightforward to see that the scaling variables x and y are always between 0 and 1. For a given Q^2 , the lowest x value is then : $x_{\min} = Q^2/s$. At HERA energies, it is possible to reach $x = 10^{-4}$ for $Q^2 = 10 \text{ GeV}^2$, a new domain at very small x , which is 100 times lower than in fixed target experiments.

2.1 Evolution equations

The structure function of the proton is one of the masterpieces of QCD. It is well known that only the Q^2 evolution and the asymptotic limits are so far given by the theory. We review below the theoretical predictions in the HERA domain.

2.1.1 Altarelli-Parisi equations

In the kinematic domain so far accessible to fixed target experiments (i.e. $x > 0.05$ for $Q^2 = 10 \text{ GeV}^2$), the Q^2 dependence of structure functions is dictated by the perturbative QCD evolution equations of (Dokshitzer-Gribov-Lipatov) Altarelli-Parisi [7][8][9]. For Non Singlet structure functions $F^{NS}(x, Q^2)$ (i.e. non flavour symmetric), the Q^2 derivative at x depends only on the quark densities at momentum fractions above x ; but for Singlet structure functions $F^S(x, Q^2)$ (i.e. flavour symmetric) the Q^2 derivative depends on both the quark and the gluon densities :

$$\frac{\partial F^{NS}(x, Q^2)}{\partial \ln(Q^2)} = \frac{\alpha_s(Q^2)}{2\pi} \int_x^1 \frac{dy}{y} F^{NS}(y, Q^2) P_{qq}^{NS}\left(\frac{x}{y}\right) \quad (4)$$

$$\begin{aligned} \frac{\partial F^S(x, Q^2)}{\partial \ln(Q^2)} &= \frac{\alpha_s(Q^2)}{2\pi} \int_x^1 \frac{dy}{y} \left[F^S(y, Q^2) P_{qq}^S\left(\frac{x}{y}\right) \right. \\ &\quad \left. + 2n_f G(y, Q^2) P_{qg}^S\left(\frac{x}{y}\right) \right] \end{aligned} \quad (5)$$

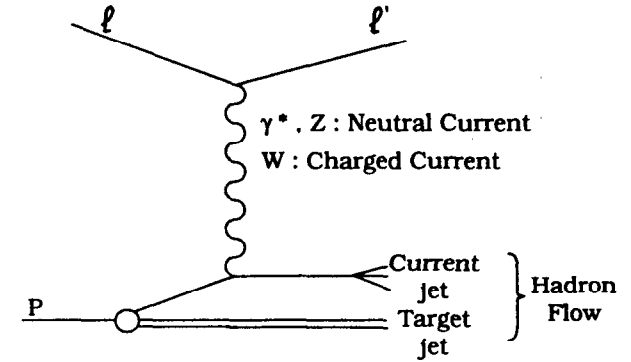


Figure 1: Basic diagram for deep inelastic scattering.

$$\frac{\partial G(x, Q^2)}{\partial \ln(Q^2)} = \frac{\alpha_s(Q^2)}{2\pi} \int_x^1 \frac{dy}{y} \left[F^S(y, Q^2) P_{gq}^S\left(\frac{x}{y}\right) + G(y, Q^2) P_{gg}^S\left(\frac{x}{y}\right) \right] \quad (6)$$

where the P_{qg} , P_{gq} and P_{gg} are the AP splitting functions, n_f is the number of flavours and $xG(x, Q^2)$ is the gluon distribution. The Q^2 evolution of the Structure Functions F_2 and xF_3 give rise to scaling violations which have been successfully tested in the most precise fixed target experiments [10][11] (for a more detailed discussion see the lectures of T. Hansl-Kozanecka and F. Sciulli in these proceedings). The scaling violations arise from the resummation of a series of $\ln(Q^2/\mu^2)$ which is a priori only valid in the kinematical domain of the Leading Log Approximation (LLA(Q^2)) defined by :

$$\begin{aligned} \alpha_s(Q^2) \ln(Q^2/Q_0^2) &\sim 1 \\ \alpha_s(Q^2) \ln(1/x) &\ll 1 \\ \alpha_s(Q^2) &\ll 1 \end{aligned} \quad (7)$$

We can see that the LLA approximation should hardly hold already at $Q^2 = 10 \text{ GeV}^2$ and $x = 0.01$ where $\alpha_s \ln(1/x) \sim 1.2$.

The AP linear evolution equations have been originally derived from a renormalization group analysis of the operator product expansion [12]. However, it is important to note that there is an other approach to the same evolution equations where quark and gluon ladders are summed, as illustrated on Fig. 2. In this summation, gluons have ordered longitudinal momenta (momentum conservation) but also strongly ordered transverse momenta

$$\begin{aligned} x &\leq x_n \leq \dots \leq x_2 \leq x_1 \\ Q^2 &\gg k_T^2 \gg k_{nT}^2 \gg \dots \gg k_{2T}^2 \gg k_{1T}^2 \gg Q_0^2 \end{aligned} \quad (8)$$

2.1.2 Lipatov equations

At very small x , but moderate Q^2 (see Fig. 3), another gluon evolution equation, still linear but which is in Leading Logarithms ($1/x$), has been derived by Lipatov and collaborators [13] in the kinematical domain defined by :

$$\begin{aligned} \alpha_s(Q^2) \ln(Q^2/Q_0^2) &\ll 1 \\ \alpha_s(Q^2) \ln(1/x) &\sim 1 \\ \alpha_s(Q^2) &\ll 1 \end{aligned} \quad (9)$$

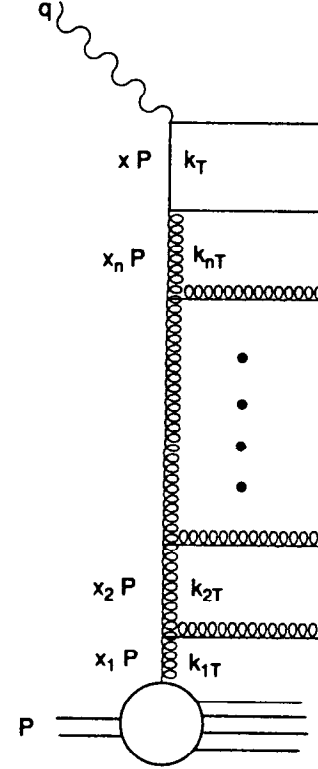


Figure 2: QCD ladder diagram describing the evolution of the gluon distribution of a proton of 4-momentum P . The contribution of quarks has been neglected for clarification.

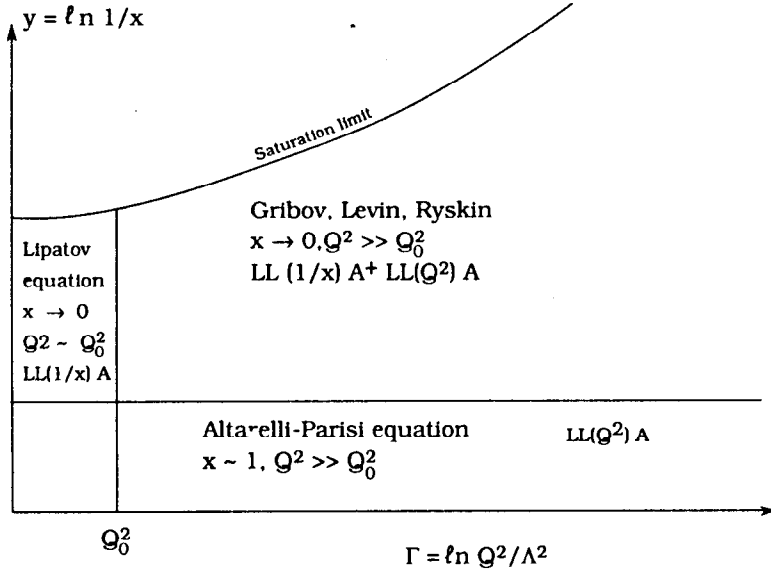


Figure 3: Theoretical regimes for deep inelastic structure functions.

Following the notations of ref [2], the Lipatov evolution equation for the gluon can be written in the form

$$f(x, k^2) = f^0(x, k^2) + \int dk'^2 K(k, k') \int_x^1 \frac{dx'}{x'} f(x', k'^2) \quad (10)$$

where

$$f(x, k^2) = \frac{\partial_x G(x, Q^2)}{\partial \ln(Q^2)}|_{Q^2=k^2} \quad (11)$$

and where the kernel

$$K(k, k') = \frac{3\alpha_s}{\pi} k^2 \left\{ \frac{1}{k'^2 |k'^2 - k^2|} - \beta(k^2) \delta(k^2 - k'^2) \right\} \quad (12)$$

with

$$\beta(k^2) = \int \frac{dk'^2}{k'^2} \left\{ \frac{1}{|k'^2 - k^2|} - \frac{1}{(4k'^4 + k^4)^{1/2}} \right\} \quad (13)$$

The non perturbative term $f^0(x, k^2)$ represents the unknown gluon proton coupling which is expected to vanish at $k^2 = 0$ and to be independent of x in the small x limit [15]. We note that the singlet quark contribution to the gluon evolution has been omitted; this approximation is justified since, as we shall see in section 4.1 the quark contribution to scaling violations is minute at $x < 10^{-2}$.

As in AP evolution, the evolution at small x can be described as a branching process in the initial state, but with different orderings [17]. In Lipatov equation, the evolution is written before the integration over the transverse momenta has been performed. In the parton chain there is no strong ordering in k_{nT}^2 but a strong ordering in x_n

$$x \ll x_n \ll \dots \ll x_2 \ll x_1 \quad (14)$$

$$Q^2 \geq k_T^2 \geq k_{nT}^2 \geq \dots \geq k_{2T}^2 \geq k_{1T}^2 \geq Q_0^2$$

The phase space has been opened. As we shall see in the next section, this will have direct impact on the final states.

2.1.3 GLR equation (first part)

The kinematical domains of validity of Altarelli Parisi and Lipatov evolution equations are a priori quite distinct (Fig. 3). However, transition between both regimes must be smooth. Gribov Levin and Ryskin have proposed a new evolution equation for the gluon, the so-called GLR equation, which involves linear and non linear terms [2]. We shall come back to the non linear part in paragraph 2.1.6.

As to the linear part of the equation, the gluonic part of the Altarelli Parisi equation has been corrected to include the kernel of the Lipatov equation. At large Q^2 , the linear term becomes the exact AP equation. At very small x only the Lipatov kernel survives. The kinematical domain of validity of the GLR equation extends the theoretical regime of perturbative QCD down to small x and large Q^2 (Fig. 3).

2.1.4 Quantitative comparisons

Although the domain of validity of the AP equations should not extend a priori down to x below $\sim 10^{-2}$, it is of practical interest to compare quantitatively AP and Lipatov evolutions in the HERA domain. It is not yet possible to study the solution of both equations by rigorous analytic calculations. However, in the Leading Log approximation, the two equations can be described by a factorised structure where the evolution is a chain of subsequent decay processes (splitting) in which partons become slower (smaller x) (Fig. 2). Such a representation can be used in Monte Carlo programs, thus allowing quantitative estimates. The gluon structure function and the multiplicity of emitted gluons were studied by Marchesini and Webber [16]. Results are shown in Fig. 4 and Fig. 5 for two types of input distributions at $Q^2 = 5 \text{ GeV}^2$, a flat distribution and a steep x variation respectively. From this study we can draw three conclusions :

1. AP and Lipatov evolution equations give similar results on the gluon inclusive distribution over a wide range of Q^2 and x , especially in the HERA kinematical domain. This similarity is due to a fortuitous cancellation of leading higher-order corrections which occurs in inclusive variables [18].
2. There are clear differences, which should be observable, in the associated multiplicity and distributions of emitted gluons between the results of the two types of input distributions and between the results of the two types of evolution algorithms.
3. The $1/\sqrt{x}$ behaviour of the gluon distribution is stable under Q^2 evolution in the two types of evolution equations. Starting from a flat distribution in x , the Q^2 evolution is fast, the x dependence becomes steeper and steeper to reach a $1/\sqrt{x}$ behaviour. Starting from a $1/\sqrt{x}$ behaviour, the x dependence evolves moderately with Q^2 .

2.1.5 Asymptotic behaviour

The numerical agreement between Lipatov and AP on the evolution of the gluon distributions does not mean that the two equations are valid at very

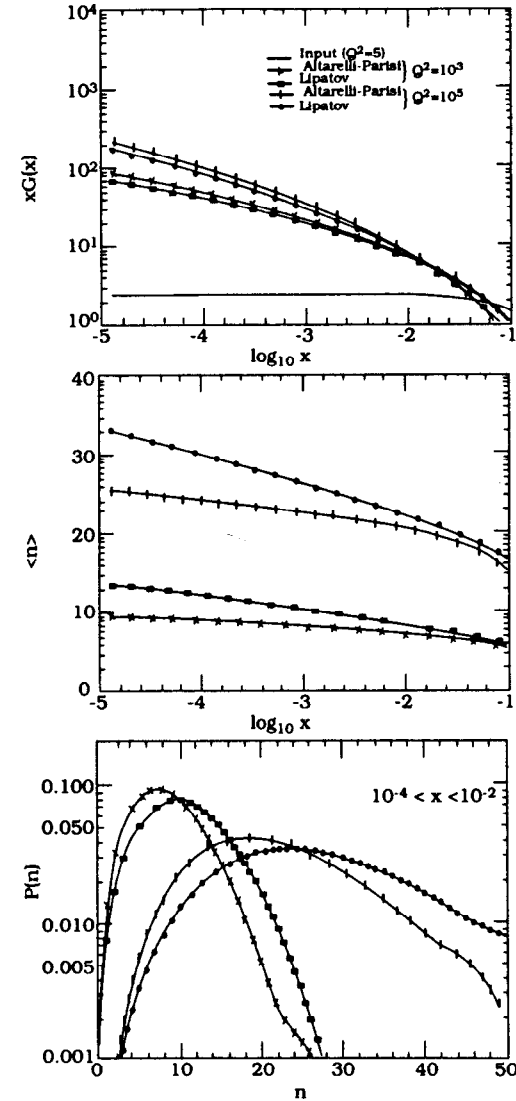


Figure 4: Monte Carlo results for a flat input structure function, $x F(x, Q^2) = A(1-x)^5$ [16].

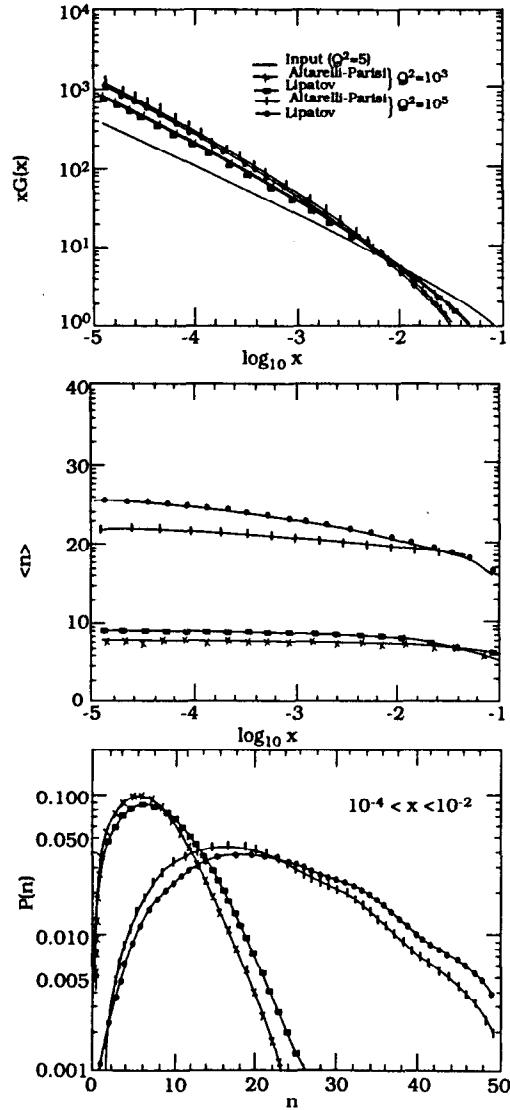


Figure 5: Monte Carlo results for a steep input structure function, $xF(x, Q^2) = Ax^{-p_s}(1-x)^5$, with $p_s = 0.626$ [16].

small x . Let us study the asymptotic limits when x goes to 0. From the standard AP equation it can be derived that in the small x limit the gluon distribution should behave as :

$$\lim_{x \rightarrow 0} xG(x, Q^2) \sim \frac{\exp \sqrt{2(\xi - \xi_0)y}}{\sqrt{2\pi} \sqrt{2(\xi - \xi_0)}} \quad (15)$$

where

$$\xi = \ln \ln \frac{Q^2}{\Lambda^2} \quad (16)$$

and

$$y \sim \ln \frac{1}{x} \quad (17)$$

The total scattering cross section of a virtual photon off a proton would then rise faster than any power of $\ln \frac{1}{x} \sim \ln \frac{s}{Q^2}$. The rise would be even faster for gluons satisfying the Lipatov evolution, where

$$\lim_{x \rightarrow 0} xG(x, Q^2) \sim h(Q^2)x^{-1/2} \quad (18)$$

The growth of the gluon density according to equations (15) and (18) can not continue forever since unitarity requires that the growth of the cross section cannot be faster than the square of the hadron radius :

$$\sigma_{tot}^{\gamma^*} = \frac{4\pi^2\alpha}{Q^2} F(x, Q^2) \leq 2\pi R(s)^2 \quad (19)$$

with the hadron radius growing like :

$$R(s) \sim \text{const.} \ln s \quad (20)$$

At very small x the rise of the gluon density must be damped by the so-called saturation mechanism.

2.1.6 Saturation and GLR equation (second part)

Two possible saturation mechanisms have been proposed. In the first approach [19] it is guessed that the High Order terms (beyond the Leading Logarithms) of the Lipatov evolution equation, although not yet fully calculated, should be sufficient to damp the gluon density up to the saturation. In the second approach, which is much more popular, a negative quadratic term is added in the evolution equation [2]. The dynamic origin of this negative term is due to interactions between different ladders, the so-called fan diagrams (for more details refer to the lecture of R.Peccei in these proceedings). A simple geometrical representation of this dynamic has also

been proposed [20] that we present below, before introducing the complete GLR equation.

By definition $xG(x, Q^2)$ is the probability density to find a gluon of longitudinal momentum x and of virtuality Q^2 times the fraction of momentum x . If we consider the rapidity $y = 1/x$ (not to be confused with the scaling variable y defined in eq.(2)), $xG(x, Q^2)$ is also the number of gluons per unit of rapidity since $dy = dx/x$.

In the infinite momentum frame, the transverse size of a gluon is $1/Q$. The density of gluons in a proton, per $dydQ^2$ cell, is then :

$$\phi \sim \frac{xG}{Q^2 R_p^2} \quad (21)$$

We have seen that the QCD evolution is a chain of parton emissions. The density of gluons increases at each splitting processes (Fig. 6) :

$$\frac{\Delta\phi}{\Delta y \Delta Q^2} \sim \alpha_s \phi \quad (22)$$

It is instructive to visualize the cascade evolution in the transverse plane, where the saturation appears when the partons start to overlap spatially and begin to interact and annihilate each other (Fig. 6). The recombination depends simply on the square of the parton density :

$$\frac{\Delta\phi}{\Delta y \Delta Q^2} \sim -(\alpha_s \phi)^2 \quad (23)$$

And at the equilibrium

$$\frac{\Delta\phi}{\Delta y \Delta Q^2} \sim \alpha_s \phi - C(\alpha_s \phi)^2 \quad (24)$$

We have now the basis for the GLR evolution equation that we can write more precisely :

$$x \frac{\partial f(x, k^2)}{\partial x} = \int dk'^2 \bar{K}(k, k') f(x, k'^2) - \frac{81\alpha_s(k^2)}{16R_p^2 k^2} [xG(x, k^2)]^2 \quad (25)$$

where $f(x, k^2)$ is defined in equation (11). We note that, as a contrast to the usual AP equations, the singlet quarks have been omitted but a similar equation can be written for sea quarks [3] and should be used for F_2 calculations. We recognize, in the linear term, the Lipatov equation (10) after differentiation over $\ln \frac{1}{x}$, and where the kernel \bar{K} has been modified to include the non singular part of the AP equation. The shadowing term in this simplified expression depends only on one free parameter R_a , which can be guessed to be between the size of the valence quark (2 GeV^{-1}) and

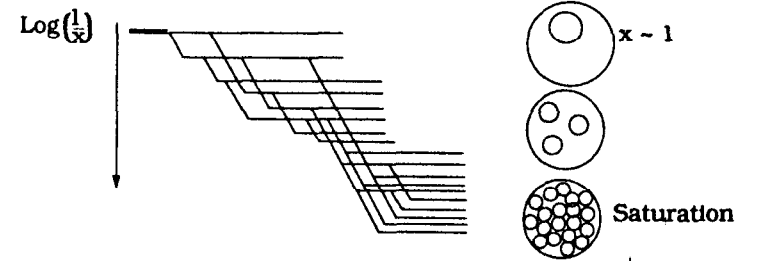


Figure 6: Structure of the parton cascade.

the size of the proton (5 GeV^{-1}), depending how locally the saturation starts, i.e. close to the valence quark or uniformly over the full transverse size of the nucleon.

An estimate on the size of the absorption correction can be inferred from the numerical calculation of the ratio of the quadratic and linear terms on the right hand side of equation (25). The results [14] for two values of R_a are presented as contours of constant W' in the (x, Q^2) plane in Fig. 7. We see that if R_a is about 5 GeV^{-1} , the absorption corrections will be hardly visible at HERA, but if R_a is about 2 GeV^{-1} they could not be missed.

At even smaller values of x we are faced to the reliability of the absorption correction. The region of validity of the GLR equation should end before saturation is reached. More contributions than fan diagrams are expected to be important beyond some boundary line [2] at very small x and low Q^2 . The separation between the GLR regime and the saturation domain is not as sharp as shown in Fig. 3, there is a transition region [21,20] which is sketched in Fig. 8. At a given Q^2 , starting from the large x values we can distinguish three different theoretical regimes :

1. regime of linear evolution equations;
2. transition region where absorption corrections are calculable in perturbative QCD;
3. non perturbative domain where saturation is reached.

2.2 Predictions on Structure Functions

A rigorous analytic solution of the GLR equation has not yet been worked out. However, different approximation methods have been developed which give definite predictions on the gluon density and on the F_2 structure function at small x . Let us review hereafter the present estimates.

2.2.1 KMRS method

A first quantitative estimate has been obtained in the frame of a Next-To-Leading-Order QCD analysis of the most recent data for deep inelastic lepton-nucleon scattering by the KMRS group [22]. A factor $x^{-1/2}$ is incorporated in the xG and $x\bar{q}$ starting distributions to approximate the Lipatov behaviour at small x without absorption corrections :

$$xG^u(x, Q_0^2) \sim C(x)x^{-1/2} \quad (26)$$

The superscript u is to indicate that G^u is the unshadowed distribution. The absorption corrections are expected to be significant at small x only.

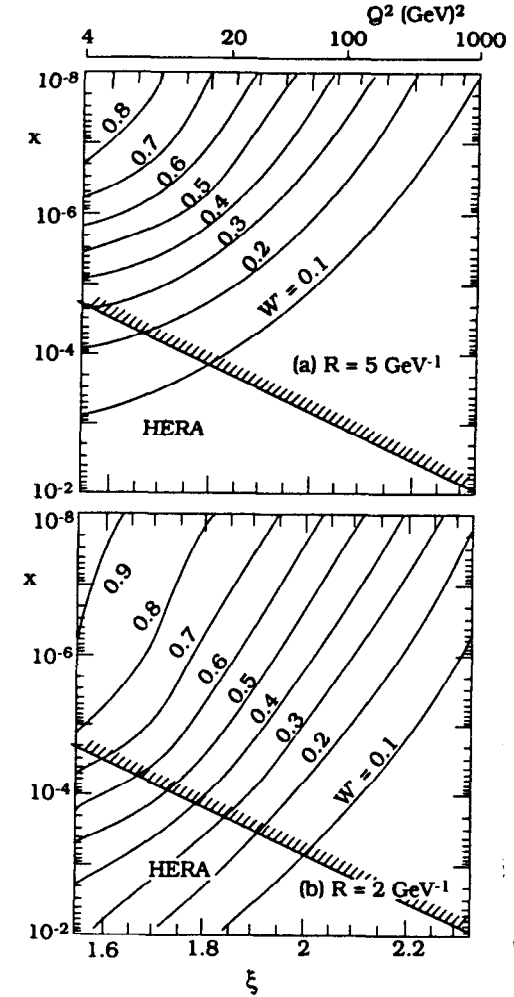


Figure 7: Contour plots of constant W' in the (y, ξ) plane where $y = \ln(1/x)$ and $\xi = \ln(\ln Q^2)$ with a) $R = 5 \text{ GeV}^{-1}$ and b) $R = 2 \text{ GeV}^{-1}$. W' is the ratio of the quadratic to the linear term of equation (25)[14].

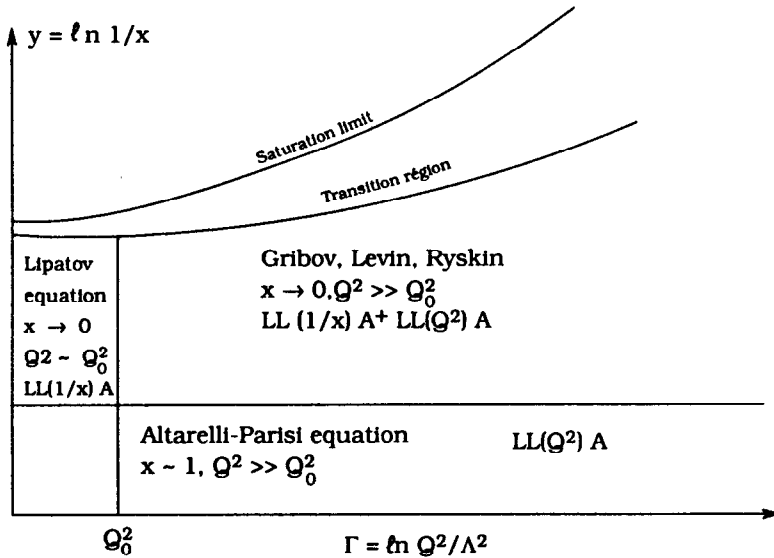


Figure 8: Theoretical regimes for deep inelastic structure functions, a more detailed sketch than in Fig.3. The transition region has been added between the linear and the saturation regions.

So, KMRS impose the absorption correction by modifying G^u for $x < x_0 = 10^{-2}$ to

$$xG(x, Q_0^2) = xG^u(x, Q_0^2) \left\{ 1 + \theta(x_0 - x) \left(\frac{C(x)x^{-1/2} - C(x_0)x_0^{-1/2}}{xG_{sat}(x, Q_0^2)} \right)^{-1} \right\} \quad (27)$$

where xG_{sat} is defined to be the gluon distribution at saturation at very small x . That is,

$$xG_{sat}(x, Q^2) = \frac{16R_a^2 Q^2}{27\pi\alpha_s(Q^2)} \quad (28)$$

The result is shown in Fig. 9 for gluons with and without absorption corrections. Here also we can see that the corrections are only significant for small values of R_a . This global fit gives also predictions on the quarks distributions and F_2 structure function. Fig. 10 shows the results for the structure function $F_2^{ep}(x, Q^2)$ at $Q^2 = 20 \text{ GeV}^2$. Although less pronounced than on the gluon distribution, the absorption corrections do affect significantly the x dependence of F_2 at $x < 10^{-3}$. The overall procedure has however been questioned [23] because once the gluon density has been calculated from the GLR equation, the gluon distribution should no longer be used in $LLA(Q^2)$ F_2 calculation.

2.2.2 KMS method

A more rigorous calculation of the gluon distribution at small x would be to compute numerical solutions of the GLR equation. The KMS [14] approach was to solve numerically a simplified GLR equation, that is the genuine Lipatov equation with non-linear shadowing terms incorporated. This simplified equation reads

$$x \frac{\partial f(x, k^2)}{\partial x} = \int_{Q_0^2}^{\infty} dk'^2 K(k, k') f(x, k'^2) - \frac{81\alpha_s(k^2)}{16R_a^2 k^2} (xG(x, k^2))^2 \quad (29)$$

where $K(k, k')$ is the Lipatov kernel defined in eq. (12). We note that, to avoid the divergence of the Lipatov kernel at $Q^2 = 0$, KMS impose an explicit lower limit Q_0^2 on the transverse momenta of the exchanged gluons. The results are shown in Fig. 11 for two different values of Q^2 , namely $Q^2 = 4$ and 100 GeV^2 . The top curve shows the gluon distribution when shadowing is neglected, from which we recognize the $x^{-1/2}$ behaviour of the Lipatov gluon. The lower two curves show the effect of the shadowing contribution assuming first, uniform shadowing in the nucleon with $R_a = 5 \text{ GeV}^{-1}$, and, second, local shadowing with $R_a = 2 \text{ GeV}^{-1}$. We see again from Fig. 11 that uniform shadowing ($R_a = 5 \text{ GeV}^{-1}$) has little impact

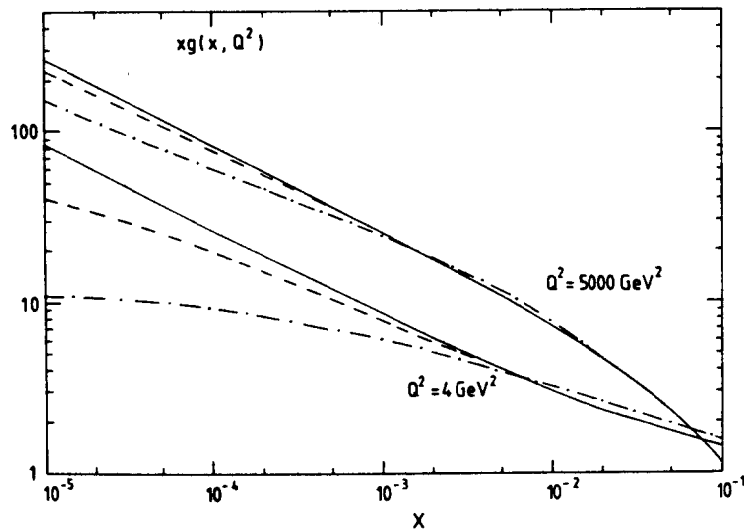


Figure 9: The gluon distribution $xG(x, Q^2)$ at $Q_0^2 = 4 \text{ GeV}^2$ (starting value) and $Q^2 = 5000 \text{ GeV}^2$ in the KMRS analysis [22]. The unshadowed gluon (B^- fit) is shown as a solid line, shadowing with $R_s = 5 \text{ GeV}^{-1}$ as a dashed line, and shadowing with $R_s = 2 \text{ GeV}^{-1}$ as a dot-dashed line.

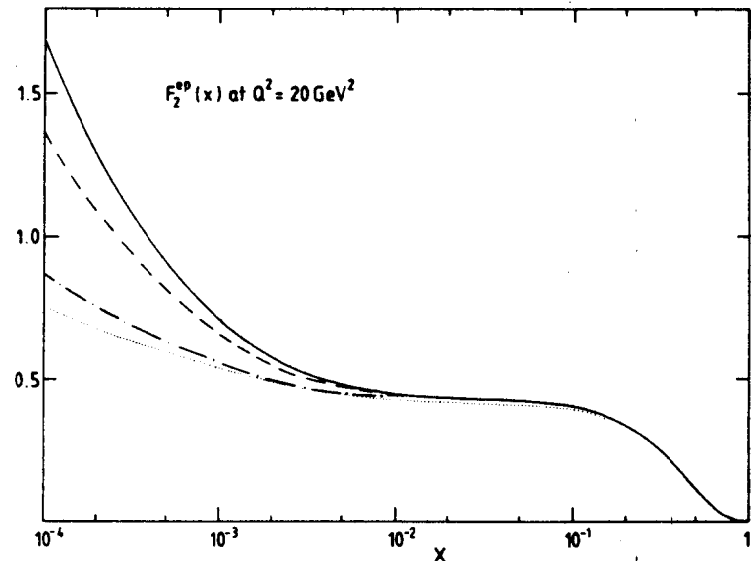


Figure 10: The structure function F_2^{ep} as a function of x at $Q^2 = 20 \text{ GeV}^2$ from the KMRS analysis [22]. The unshadowed F_2 (B^- fit) is shown as a solid line, shadowing with $R_s = 5 \text{ GeV}^{-1}$ as a dashed line, and shadowing with $R_s = 2 \text{ GeV}^{-1}$ as a dot-dashed line. For comparison, the prediction for the B_0 set of partons, generated from a flat input distribution, is drawn as a dotted line.

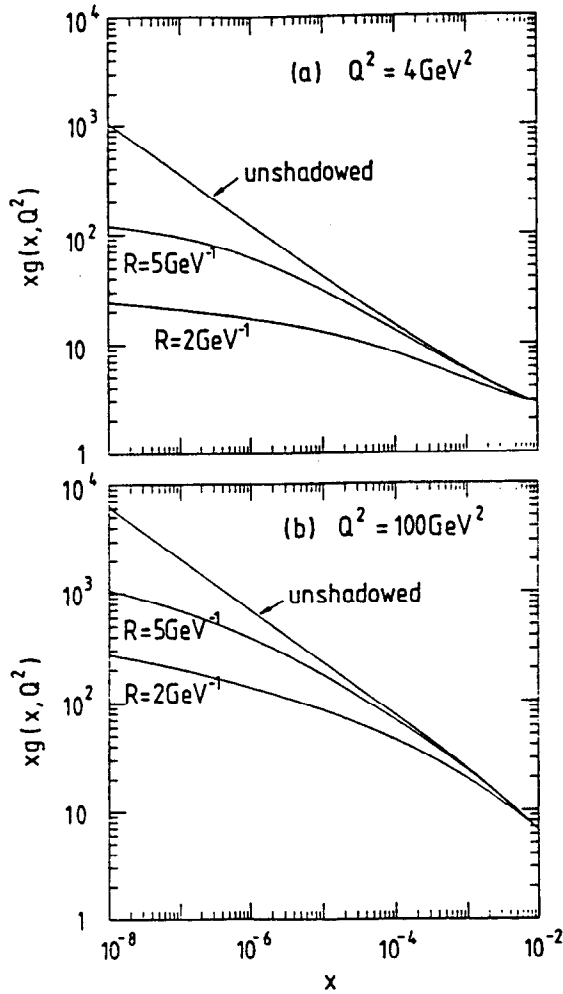


Figure 11: The values of $xG(x, Q^2)$ at (a) $Q^2 = 4 \text{ GeV}^2$ and (b) $Q^2 = 100 \text{ GeV}^2$ from the KMS analysis [14]. In each figure the three curves are, in descending order, the solution with shadowing neglected and the solutions with the shadowing term included with $R_s = 5 \text{ GeV}^{-1}$ and $R_s = 2 \text{ GeV}^{-1}$.

on the behaviour of the gluon distribution in the region $x > 10^{-4}$. The gluon distributions from [14] are also compared with those of the B_- set of KMRS [22] in Fig. 12. There is an agreement on the shape of the very small x behaviour of the gluon between the two procedures (KMS and KMRS), whether or not the shadowing corrections are included. However the Q^2 evolution is faster in the KMS than in the KMRS analysis. This difference is not surprising because the Lipatov equation is not supposed to be valid at high Q^2 .

2.2.3 BBS method

Numerical analysis can also be performed on the GLR equation directly. In the BBS [21] analysis of the gluon distribution, two very different input distributions have been tried, a distribution which approaches a constant at small x [26] and a distribution with a much steeper variation in $x^{0.33}$ [24] respectively. Both input distributions are shown in Fig. 13a. Two extreme cases have been considered, namely $R_s = 2 \text{ GeV}^{-1}$ and $R_s = 6.3 \text{ GeV}^{-1}$, corresponding to a factor ten difference on the $1/R_s^2$ factor in the GLR equation (25). The results are given in Fig. 13b-d. The most striking feature is that at a given Q^2 the same gluon distribution can be achieved either from a steep input distribution evolved at high Q^2 with shadowing terms or from a flat input evolved without shadowing.

Another way to illustrate the ambiguity of the F_2 or gluon interpretation is to consider the variety of parametrisations of xG or F_2 in the HERA domain [22,24,25,26] which are shown in Fig. 14. The large spread of variation at fixed Q^2 or even at fixed $y = Q^2/sz$ (more adapted to HERA kinematics, see section 3.5) is related to various assumptions on the two input quantities : the starting distribution and the size of the shadowing corrections. We see that, in some cases (for example KMRS B_-), even when the gluon distribution is steep, the structure function F_2 may appear to be flat at small x . The only chance to detect the presence of absorption terms from F_2 measurement would be to analyse the Q^2 evolution. At the time of this lecture the studies are still going on. The results will be presented in reference [27].

2.3 Dedicated processes

2.3.1 Hot Spots

In the model of Gribov-Levin-Ryskin, the saturation can occur either on the whole face of the proton or on a smaller region of the proton called [28] a hot spot. A. Mueller has proposed a method to detect directly such hot spots. The experimental procedure consists in looking at selected jets associated

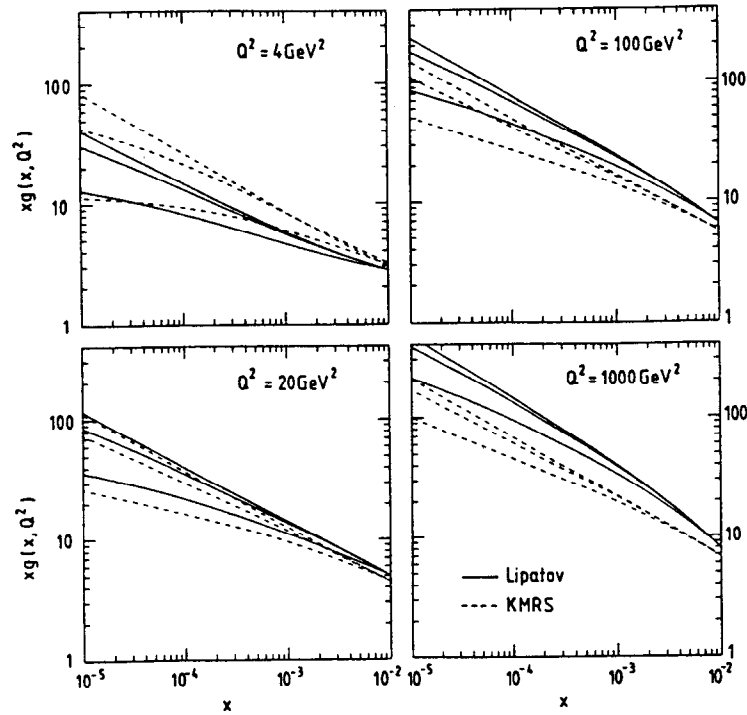


Figure 12: The continuous curves are the values of $xG(x, Q^2)$ determined by solving the Lipatov equation (exactly as in Fig. 11) for $Q^2 = 4, 20, 100, 1000 \text{ GeV}^2$ [14]. The dashed curves are $xG(x, Q^2)$ of set B_- of the KMRS [22] analysis with and without shadowing.

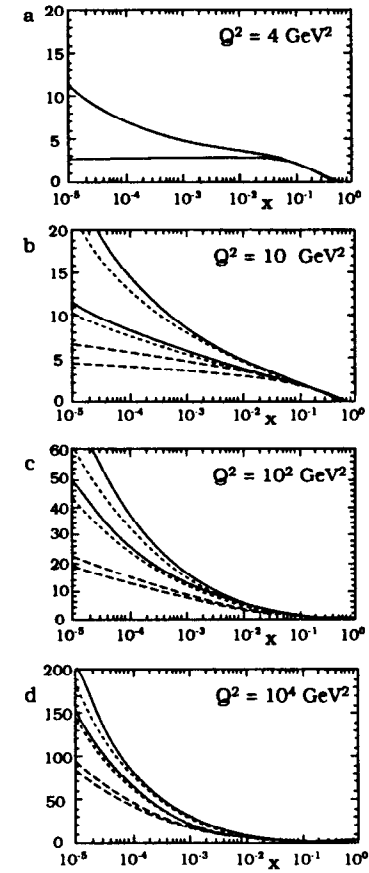


Figure 13: a) The MT and EHLQ input distribution $xG(x, Q_0^2)$ of Morfin-Tung [24] (upper curve) and Eichten et al. [26] (lower curve). b-d) Gluon density after evolution at various values of Q^2 from the BBS analysis [21]. The drawn lines belong to the linear equation without shadowing, the dashed (dotted) ones to the non linear case with $R_s = 6.3 \text{ GeV}^{-1}$ ($R_s = 2 \text{ GeV}^{-1}$). Upper (lower) curves stem from the MT (EHLQ) input distributions.

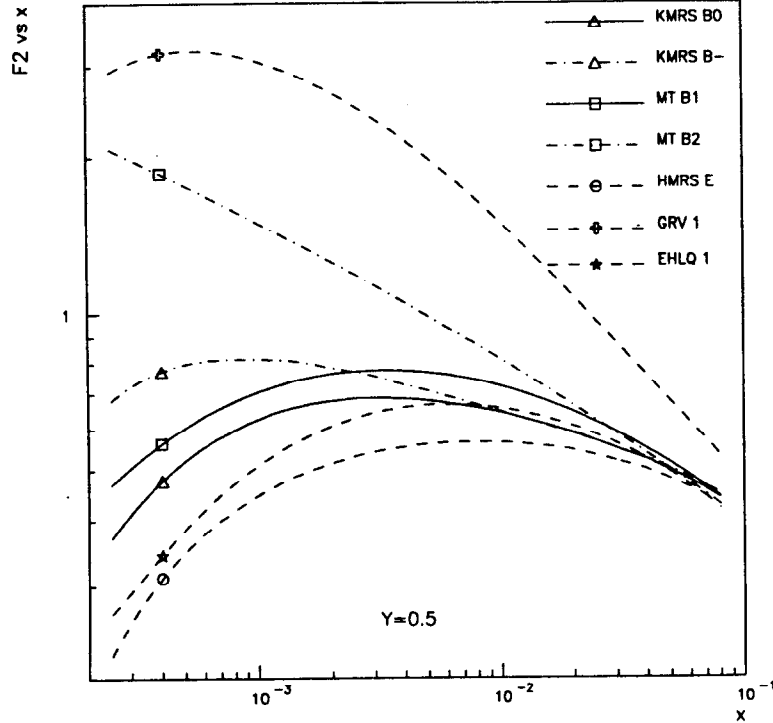


Figure 14: $F_2(x, Q^2)$ at $y = 0.5$ and HERA nominal energies.

with a deep inelastic event as sketched in Fig. 15. The transverse size $1/k_{1t}$ of the selected jet should not be much larger than $1/Q$ the transverse size of the virtual photon, in order to be sensitive to the jets produced around the struck parton. The momentum fraction x_1 of the jet should be as large as possible whereas the momentum fraction x_B of the struck quark should be small as possible in order to explore the region $x_B \ll x_1$. The associated cross section reads

$$\frac{k_{1t}^2 x_1 dF_2(x_1, k_{1t}^2)}{dx_1 dk_{1t}^2} = C \alpha_s(Q^2) \left[x_1 G(x_1, k_{1t}^2) + \frac{4}{9} (x_1 q(x_1, k_{1t}^2) + x_1 \bar{q}(x_1, k_{1t}^2)) \right] \frac{\exp\left(\frac{12\alpha_s(Q^2)}{\pi} \ln 2 \ln \frac{x_1}{x_B}\right)}{\sqrt{\ln \frac{x_1}{x_B}}} \quad (30)$$

where C is a calculable constant.

We note that this formula predicts a steep rise of the cross section as the ratio x_B/x_1 becomes small. Because k_{1t} is close to Q , the non selected jets all occupy the same spot in the proton, an area of size $4\pi/Q^2$, as the selected jet k_{1t} does. In a hot spot, as x_B/x_1 becomes smaller and smaller, the saturation should start and a weakening of the x -growth should set in. Studies on experimental detection of the selected jet (k_{1t}, x_1) are promising and will be reported in ref[29].

2.3.2 Diffractive dissociation of virtual photons

M.Ryskin [30] suggests to study the diffractive dissociation of the virtual photon into three jets : quark, antiquark and gluon (see Fig. 16). The important feature is that, when the rapidity gap between the forward gluon jet (x_k, k_t^2) and the proton is large ($\delta y > 4$), the cross section is proportional to $[x_k G(x_k, k_t^2)]^2$ and thus especially sensitive to the saturation effects. As a numerical example for :

$$\begin{aligned} Q^2 &\sim 30 - 100 \text{ GeV}^2 \\ M^2 &\sim 300 - 1000 \text{ GeV}^2 \\ x_B &\sim 0.3 - 1 \cdot 10^{-3} \end{aligned} \quad (31)$$

where M^2 is the squared invariant mass of the gluon-quark-antiquark system and (Q^2, x_B) are defined at the leptonic vertex. The cross section without shadowing amounts to about $2 - 10 \text{ nb}$ and can be reduced to 0.01 nb when the saturation mechanism set in.

2.3.3 Correlation Functions

Another method to detect the saturation mechanism has been proposed by E.Levin [20]. The idea is to look at correlation in rapidity for any pair of

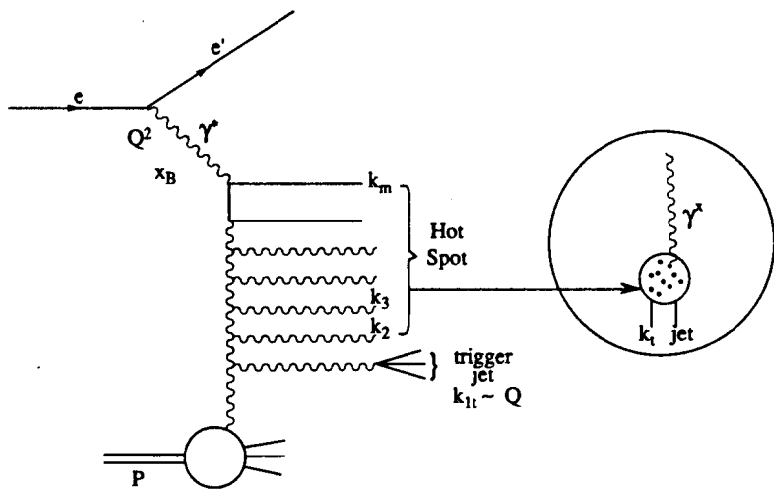


Figure 15: The hotspot hunting selection.

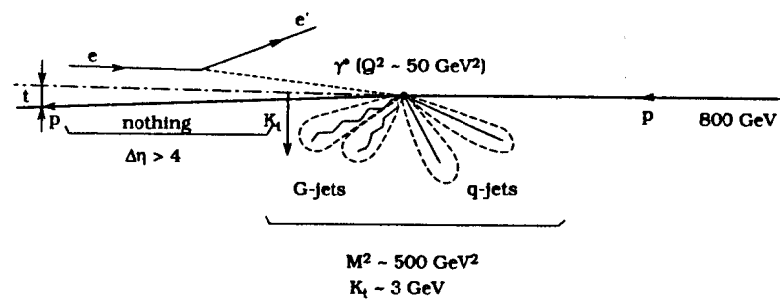


Figure 16: Diffractive dissociation of the virtual photon into gluon and quark jets.

hadrons in the detector

$$R(y_1, y_2) = \frac{\frac{1}{\sigma_{tot}} \frac{d\sigma}{dy_1 dy_2}}{\frac{1}{\sigma_{tot}} \frac{d\sigma}{dy_1} \frac{1}{\sigma_{tot}} \frac{d\sigma}{dy_2}} - 1. \quad (32)$$

The correlation has actually two components

$$R(y_1, y_2) = R_{SR} + R_{LR} \quad (33)$$

R_{SR} , the short range correlation, is related to the usual AP evolution mechanism [31] and decreases strongly when $\Delta y (= y_1 - y_2)$ gets large. R_{LR} , the long range correlation is related to the absorption processes. At $x \sim 10^{-3}$ and $Q^2 \sim 100 \text{ GeV}^2$ the correlation is expected to be as large as 50% for $\Delta y > 4$. The actual signature depends on the hadronization of the partons and has not been yet fully worked out.

3 Measurement of Q^2 and x

We have seen in the paragraph (2.2) that, at HERA energies, it is possible to reach a new domain at very small x , which is 100 times lower than in fixed target experiments. It is furthermore possible to reach a new domain at very high Q^2 which is also about 100 times higher than in fixed target experiments. In this section we discuss which part of the (Q^2, x) domain is actually accessible to experiments where statistical and systematic errors could be kept below 10 %.

3.1 Rates

At high Q^2 , the outgoing lepton can be an electron (neutral current) or a neutrino (charged current) (Fig. 1). In order to evaluate the expected rates, we have to define a bin size in Q^2 and x . Hereafter we take four bins per decade in x and four bins per decade in Q^2 and an integrated luminosity of 100 pb^{-1} . The contours of the bins which contain at least 100 events are drawn in Fig.17 for neutral and charge current interactions. We note that in neutral current interactions the rates are large enough in the whole (Q^2, x) region open by the kinematics, except at the very large x ($x > 0.6$), very high Q^2 corner ($Q^2 > 30000 \text{ GeV}^2$). On the contrary, the rates of charged current events are negligible at low x or at moderate Q^2 . The only regions where the rates are significant are at $Q^2 > 300 \text{ GeV}^2$ and $x > 0.01$ but excluding the very large x very high Q^2 corner as in neutral current interactions.

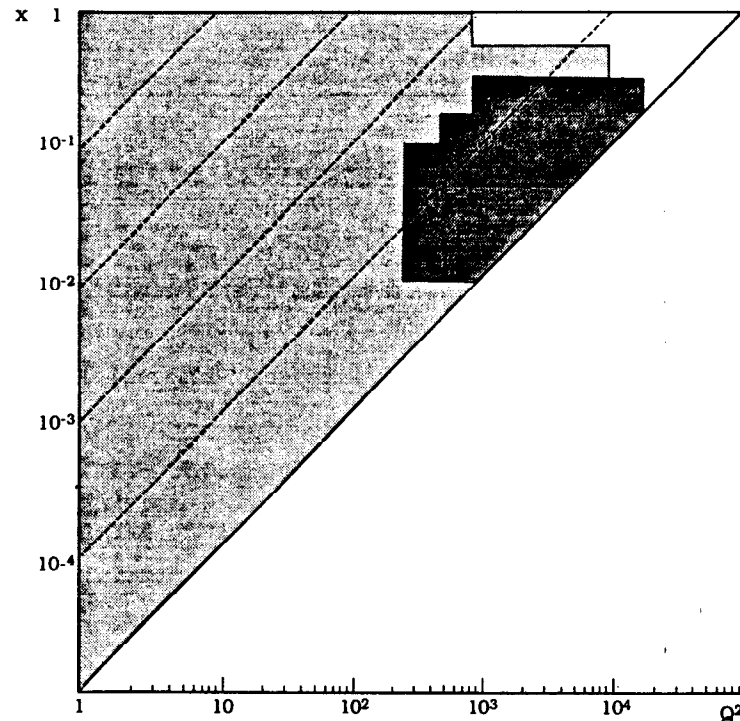


Figure 17: Contours of $(\log x, \log Q^2)$ bins (4 bins per decade in x and Q^2) which contain more than 100 events in neutral current interactions (pale shaded area) and charged current interactions (dark shaded area). Estimates done for an integrated luminosity of 100 pb^{-1} and with the EHLQ parametrization [26].

3.2 Electron measurement

In charged current events, since the outgoing lepton is a neutrino, the kinematics can only be reconstructed from the hadrons. In neutral current events, the kinematics can be reconstructed by using either the scattered electron or the hadron flow or both. Let us consider first the case of the electron measurement. Q^2 and y can be easily expressed in terms of the scattered electron energy E'_e and angle θ_e in the laboratory frame :

$$\begin{aligned} Q^2 &= 4E_e E'_e \cos^2(\theta_e/2) \\ y &= 1 - \frac{E'_e}{E_e} \sin^2(\theta_e/2) \end{aligned} \quad (34)$$

where θ_e , the scattering angle, is defined to the proton direction. x can be deduced from Q^2 and y by the relation (3).

A first limitation of the kinematical range is introduced by the beam pipe which at present excludes angles to the electron beam direction below about 7 degrees for tracking and calorimetry measurement. There is however hope to reduce the diameter of the beam pipe by about a factor two at a later stage. Lines of constant scattered angle and energy are drawn in Fig. 18. We see that the angular limit introduces a cut at small Q^2 , $Q^2 = 4E_e^2 \cos^2(\theta_e/2) \sim 13.5 \text{ GeV}^2$, in most of the x region except at the very small x values where one can reach lower Q^2 values.

From relation (34) we see that Q^2 can be reconstructed with a good precision (a few per cent) in the whole kinematical range with any modest calorimeter. The main difficulty is the x determination, where the $1/y$ enhancement factor in the x resolution,

$$\delta x/x = 1/y \delta E'_e/E'_e \quad (35)$$

implies that the smearing induced even by a good sampling calorimeter of resolution $\delta E'_e/E'_e = 0.10/\sqrt{E'_e}$ can only be kept under control (i.e. below 20 %) for y above 0.1. The resolution is however not the largest source of error in structure functions measurement. Even more important is the energy scale. A systematic calibration error of 1% in the energy of the calorimeter generates a systematic shift on the differential cross section which rises as the inverse power of y and reaches already 10% at y around 0.1 [32,33]. From a measurement of the electron energy with a sampling calorimeter, it is likely that the systematic errors on the structure functions can only be kept below 10% for y above at least 0.1 [32].

3.3 Hadron flow measurement

A method to determine x and Q^2 in charged current events has been proposed by A. Blondel and F. Jacquet [34]. From energy-momentum con-

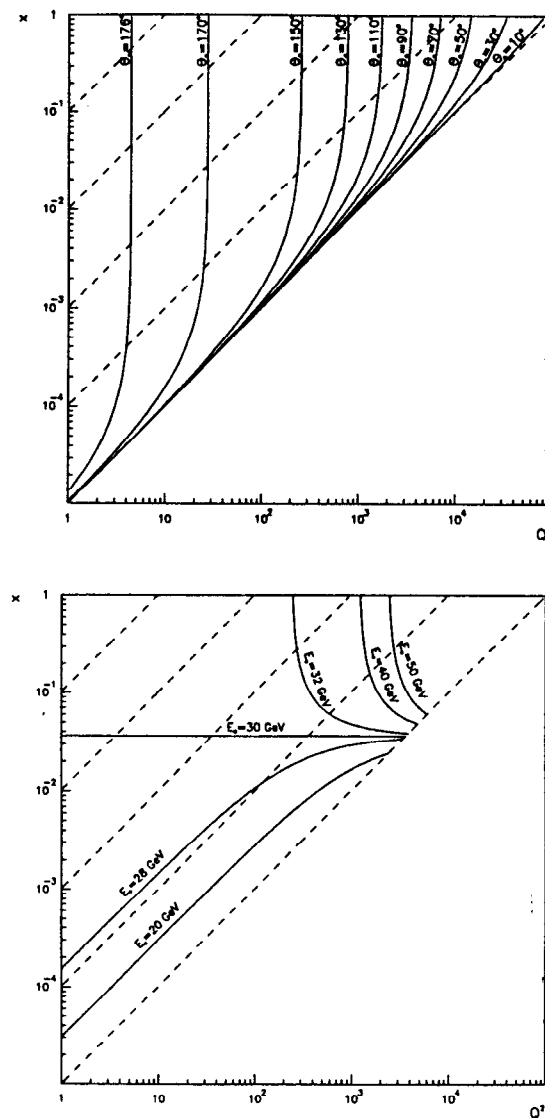


Figure 18: a) Lines of constant scattered electron angle to the proton direction. b) Lines of constant scattered electron energy.

servation, it is straightforward to express y and Q^2 as a function of the laboratory variables of the outgoing hadrons :

$$y = \frac{\sum_h (E_h - p_{zh})}{2E_e}$$

$$Q^2 = \frac{P_t^2}{(1-y)} = \frac{(\sum_h \vec{p}_{th})^2}{1-y} \quad (36)$$

where E_h, p_{zh} and \vec{p}_{th} are the energy, longitudinal momentum (in the proton direction) and transverse momentum of the hadron h respectively. P_t is the total transverse momentum of the outgoing hadron flow. We note that the total hadron flow enters in both expressions. No assumption is made on the internal structure of the proton. It is not necessary to identify, amongst the outgoing hadrons, the current jet coming from the interaction of the virtual boson with the struck quark in the proton. In a calorimeter the summation on hadrons can be replaced by a summation on towers.

We also note that particles emitted in the forward (proton) direction do not contribute to Q^2 and y . Reconstruction errors depend mainly on three effects : the size of the beam hole, the errors on the angle and the errors on the energy of the outgoing hadrons. Detailed Monte Carlo studies have shown that the salient features of the experimental errors can be inferred by considering the kinematics in the laboratory frame of a current jet of pencil type. Lines of constant current jet energies and constant jet angles are drawn in Fig. 19. We can see that at small x the jet energies are small and that, as x rises, the current jet is emitted more and more in the forward direction. This is easily understood, if we remember that x is the fraction of proton momentum carried by the struck parton. To be more quantitative, let us consider the following partial derivatives, where the angle θ_J is the polar angle of the current jet :

$$\delta x/x = (-2 \cot(\theta_J) + ((1-2y)/(1-y)) \cot(\theta_J/2)) \delta \theta_J$$

$$\delta Q^2/Q^2 = (2 \cot(\theta_J) + y/(1-y) \cot(\theta_J/2)) \delta \theta_J \quad (37)$$

The resolution in the forward direction is very poor due, first, to the $\cot(\theta_J/2)$ and $\cot(\theta_J)$ terms and, second, to the loss in the beam pipe. The measurement of charged current events will then be restricted to events with a current jet angle above about 10 degrees.

The sensitivity to the energy resolution can be seen in the expressions of the energy partial derivatives :

$$\delta x/x = 1/(1-y) \delta E_J/E_J$$

$$\delta Q^2/Q^2 = (2-y)/(1-y) \delta E_J/E_J \quad (38)$$

where E_J is the energy of the current jet. The resolution on Q^2 and x is clearly poor at large y or at low jet energy. The variable x is twice

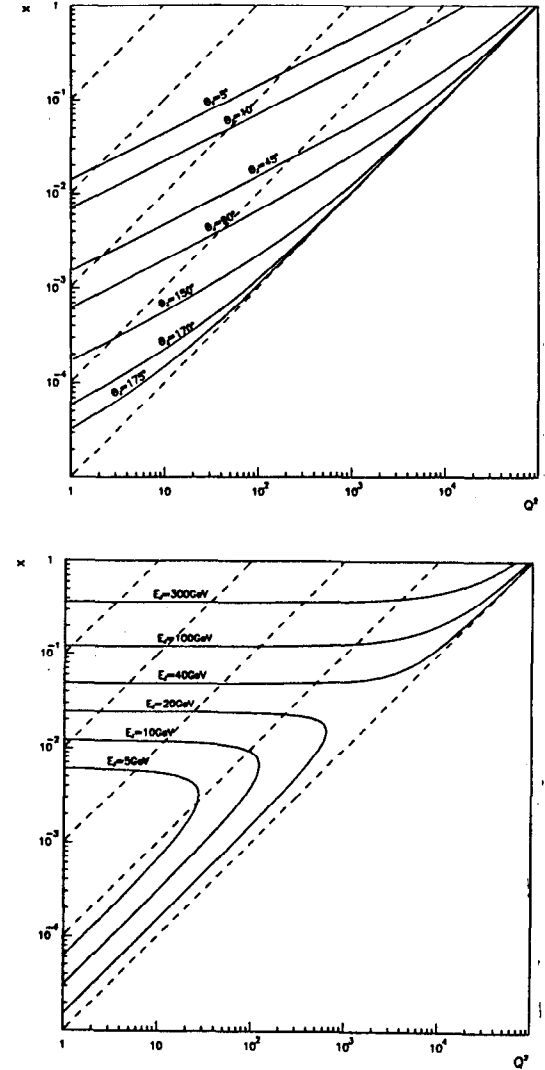


Figure 19: a) Lines of constant current jet angle to the proton direction in the laboratory frame. b) Lines of constant current jet energy.

less sensitive to the energy resolution than the variable Q^2 . So, requiring the resolution on the measurement of Q^2 and x to be better than $\sim 20\%$ excludes the region at large y ($y > 0.7$) and the region at small x ($x < 10^{-2}$) [32].

3.4 Combining electron and hadrons

In neutral current events, electron and hadron measurement can be combined to improve the determination of x and Q^2 . An obvious combination is to get Q^2 from the electron measurement and x from the hadron flow measurement. Compared to the electron measurement which is limited at $y \sim 0.1$, this mixed measurement allows to lower the y limit down to $y \sim 0.01$ in the x region around 0.01, that is $5 \cdot 10^{-3} < x < 5 \cdot 10^{-1}$ (Fig. 18). More sophisticated combinations have been proposed which will be discussed in details in the proceedings of the 1991 HERA workshop. Those combinations give similar resolutions to the naive one (x from hadrons, Q^2 from electrons) but with different systematics. A good example is the so-called "Two Angles" method :

$$\alpha_e = \frac{E'_e - p'_{ez}}{p_{te}} = \frac{(1-y) E_e}{xy E_p}$$

$$\alpha_H = \frac{\sum_h (E^h - p_{zh})}{|\sum_h (\vec{p}_{th})|} \quad (39)$$

where x and y are reconstructed from α_e and α_H . We note that α_e depends only on the electron angle and not on the electron energy and that α_H is weakly sensitive to the measurement of the hadron energy.

What is even more important when combining electron and hadron is the reduction of the radiative corrections, that is the size of

$$\delta_{corr} = \frac{d^2\sigma/dxdy}{d^2\sigma/dxdy|_{Born}} - 1 \quad (40)$$

A detailed discussion of the radiative processes in ep scattering is beyond the scope of this lecture. Let us just briefly mention that the radiative corrections are much smaller when x and Q^2 are reconstructed from the hadron flow or from a combination of electron and hadrons than when they are reconstructed from the scattered electron only [1].

3.5 Accessible domains

To summarize the discussion on measurement of inclusive scattering at HERA we have sketched on Fig. 20, the contours of the (Q^2, x) region where the systematic errors should be below 10% with either of the three methods

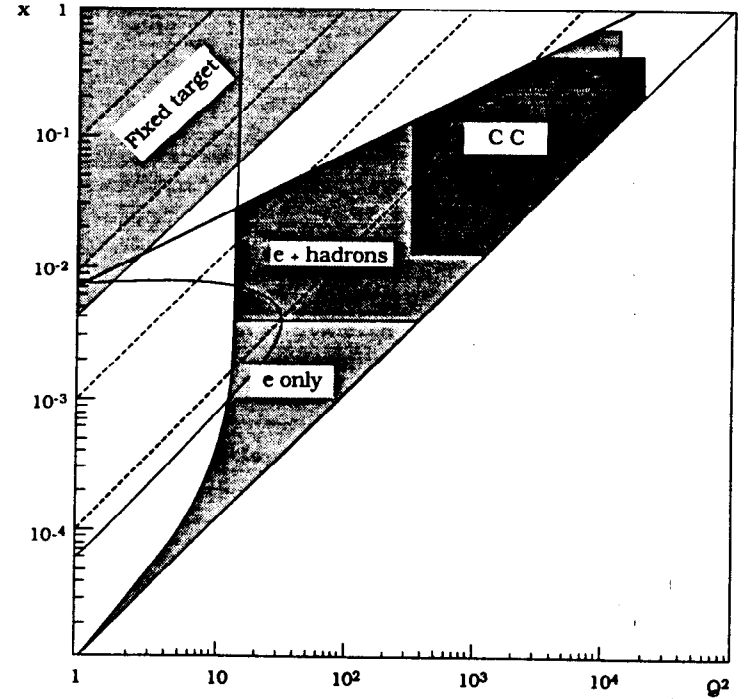


Figure 20: Accessible domain at HERA nominal beam energies ($30 \text{ GeV} \times 820 \text{ GeV}$), for an integrated luminosity of 100 pb^{-1} . The bold lines surround the bins (4 bins per decade in x and Q^2) where systematic and statistical error can be kept below 10% in Charged Current events ("CC") and Neutral Current events ("e only" and "e + hadrons").

of measurements. In the case of charged current events it is necessary to restrict even more the accessible domain by asking $P_i > 10 \text{ GeV}$ in order to trigger efficiently on the missing scattered neutrino. We note that there is no overlap with the data accumulated in fixed target experiments. However some overlap could be possible by lowering the energy of the proton beam or (and) of the electron beam.

4 Gluon determination and QCD tests

An important feature from all QCD analyses of the deep inelastic data in fixed target experiments is that the gluon distribution is very poorly determined at small x ($x < 0.1$) [35]. Several methods have been proposed to measure the gluon distribution at small x at HERA. A first method is based on the description of scaling violations by the QCD evolution equations, that we have discussed in section (2). A second method relies on the QCD interpretation of the longitudinal structure function F_L . A third method is related to the production of heavy quarks by photon-gluon fusion processes. Let us review the anticipated precisions of these methods, starting by the well known scaling violations.

4.1 Scaling Violations

At HERA energies, the differential Neutral Current (NC) cross section depends on three structure functions :

$$\frac{d^2 \sigma_{NC}(e^\mp)}{dx dQ^2} = \frac{4\pi\alpha^2}{xQ^4} \left[y^2 x F_1(x, Q^2) + (1-y) F_2(x, Q^2) \pm (y - \frac{y^2}{2}) x F_3(x, Q^2) \right] \quad (41)$$

In the standard parton model $F_2 = 2xF_1$ (Callan Gross relation [36]) and the two structure functions F_2 and xF_3 are given by :

$$F_2(x, Q^2) = \sum_{f=1}^{n_f} A_f(Q^2) [xq_f(x, Q^2) + x\bar{q}_f(x, Q^2)] \quad (42)$$

$$xF_3(x, Q^2) = \sum_{f=1}^{n_f} B_f(Q^2) [xq_f(x, Q^2) - x\bar{q}_f(x, Q^2)] \quad (43)$$

where the sum is over all n_f flavours in the proton and q_f (\bar{q}_f) are the probabilities to find a quark (antiquark) in the proton carrying the momentum fraction x . The coefficients A_f and B_f depend on the couplings of the

fermions f to the neutral current :

$$A_f(Q^2) = e_f^2 - 2e_f v_e v_f P_Z + (v_e^2 + a_e^2)(v_f^2 + a_f^2) P_Z^2 \quad (44)$$

$$B_f(Q^2) = -2e_f a_e a_f P_Z + 4v_e v_f a_e a_f P_Z^2 \quad (45)$$

where e_f is the electric charge, v_f and a_f are the NC axial and vector couplings of the fermions. P_Z is the propagator ratio $P_Z = Q^2/(Q^2 + M_Z^2)$. This ratio is very small at low Q^2 where $Q^2 \ll M_Z^2$, making the xF_3 contribution to the neutral cross section negligible in fixed target experiments. However at HERA, even in the large x large Q^2 domain where the Callan Gross relation is supposed to be valid ($F_2 = 2xF_1$), the cross section is still a function of the two structure functions F_2 and xF_3 which can only be disentangled by combining electron and positron measurements :

$$F_2(x, Q^2) = \frac{1}{2} [\bar{\sigma}_{NC}(e^-) + \bar{\sigma}_{NC}(e^+)] \quad (46)$$

where

$$\bar{\sigma}_{NC}(e^\mp) = \frac{xQ^4}{2\pi\alpha^2 [1 + (1-y)^2]} \frac{d^2 \sigma_{NC}(e^\mp)}{dx dQ^2} \quad (47)$$

Nevertheless, it has been noted [37] that there is a partial cancellation of the Z contributions to F_2 and xF_3 in $\bar{\sigma}(e^+)$, such that, to a very good approximation,

$$F_2^{em}(x, Q^2) = \bar{\sigma}_{NC}(e^+) \quad (48)$$

where F_2^{em} is the familiar electromagnetic structure function,

$$F_2^{em}(x, Q^2) = \sum_{f=1}^{n_f} e_f^2 (xq_f + x\bar{q}_f) \quad (49)$$

As is shown in Fig. 21, for an integrated luminosity of 100 pb^{-1} , the difference between $\bar{\sigma}(e^+)$ and F_2^{em} is smaller than the statistical error except in the high y , high Q^2 domain

$$\begin{aligned} Q^2 &> 2500 \text{ GeV}^2 \\ y &> 0.55 \end{aligned} \quad (50)$$

To assess the significance of the QCD analysis of the scaling violations, the following simplifications have been made [37] :

- keep only the part of the (x, Q^2) plane accessible to measurement of either the scattered electron measurement or the hadron flow, but not using the extension brought by combining electron and hadron measurement .

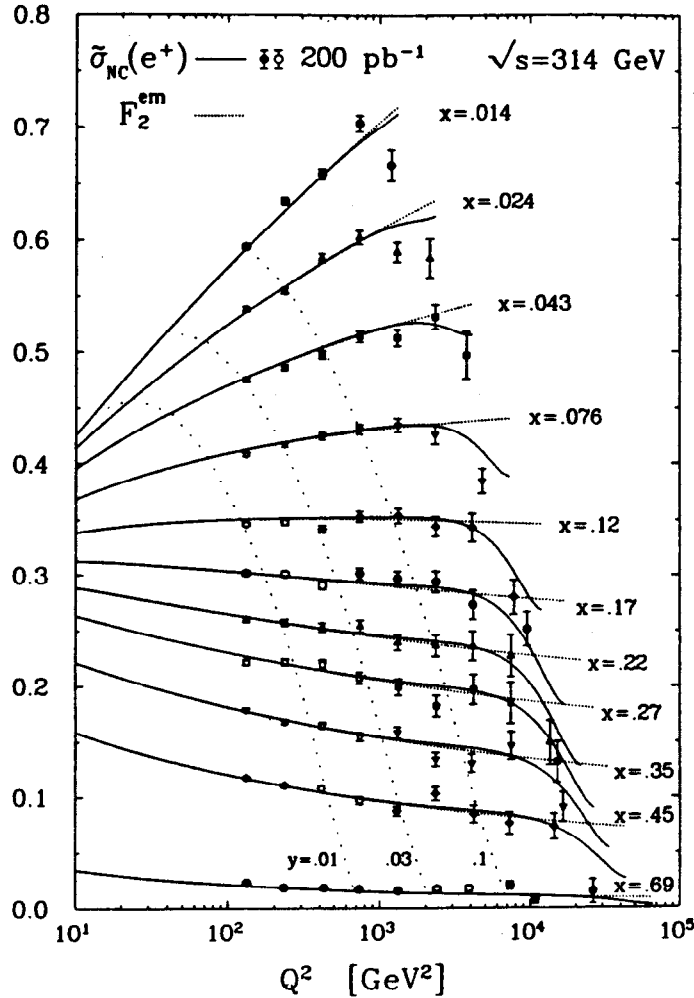


Figure 21: Differential cross section at $x > 0.01$ from reference [35]. The full (open) points show the results obtained from electron(hadron) measurements and correspond to 200 pb^{-1} . The full curves are theoretical predictions on the observable $\tilde{\sigma}_{NC}(e^+)$, while the dotted curves are the corresponding expectations on the electromagnetic structure function F_2^{em} .

- do not try to separate the scaling violations due to the Z propagator (eq. 44) from those due to QCD evolutions and by then restricting the analysis to the domain defined in equations (50).
- do not try to fit the non linear absorption corrections but rather use the Altarelli Parisi evolution equations (4,5,6), that we have seen (remember Fig. 5 and 4) to give similar results to the Lipatov equation on the gluon distribution in the HERA domain.

In the Quark Parton Model, the proton structure function F_2 is a sum of Singlet (i.e. flavour symmetric) and Non Singlet terms :

$$F_2^{em}(x, Q^2) = \frac{5}{18} x F^S(x, Q^2) + \frac{1}{6} x \Delta_p(x, Q^2) \quad (51)$$

where

$$x F^S = \sum_{f=1}^{n_f} (q_f + \bar{q}_f) \quad (52)$$

$$x \Delta_p = \sum_{i=1}^{n_f/2} (u_i + \bar{u}_i - d_i - \bar{d}_i) \quad (53)$$

Therefore, in QCD fits of the scaling violations in e-p scattering, the free parameters are not only Λ (or equivalently α_s) but also the input gluon distribution which is not directly measurable but appears in the evolution of all Singlet distributions (eq. 5 and 6), while the quark input distributions are given by the data. At large x ($x > 0.25$), the contribution of the gluon to the evolution of F_2 is much smaller than that of the valence quarks, as illustrated in Fig. 22. Only a Non Singlet fit has to be performed. However, even with an integrated luminosity of 200 pb^{-1} , the resulting statistical precision on Λ is rather modest (see Table 1).

Extending the analysis down to $x = 0.01$ does not improve the precision on α_s , because at the same time the input gluon distribution has also to be fitted. It is moreover obvious from the expressions for the evolution of singlet distributions that α_s and the input gluon distribution are strongly correlated (see equations (5 and 6)). This correlation has been studied [38] by assuming a simple parametrisation of the input gluon distribution :

$$x G(x, Q_0^2) = A(\nu, \lambda) x^{-\lambda} (1-x)^\nu (1+9x) \quad (54)$$

We can see in Fig. 23 how large the correlation is. Λ varies monotonously with λ and ν . On the other hand, if we assume that at the time of the QCD analysis of the deep inelastic scattering at HERA, the gluon distribution has been determined by other means, then the achieved statistical precision on Λ (10%) or on α_s (3%) would be competitive to other measurements.

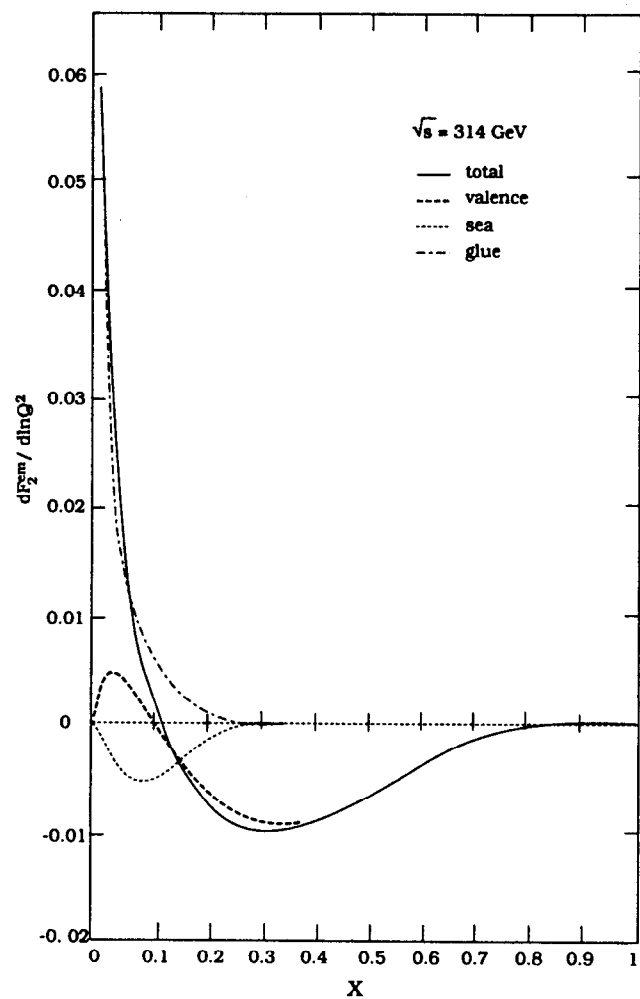


Figure 22: Evolution of the structure function F_2^{em} . The contributions from valence quarks, sea quarks and gluons are shown separately for the unrestricted y range and $Q^2 > 100 \text{ GeV}^2$ [35].

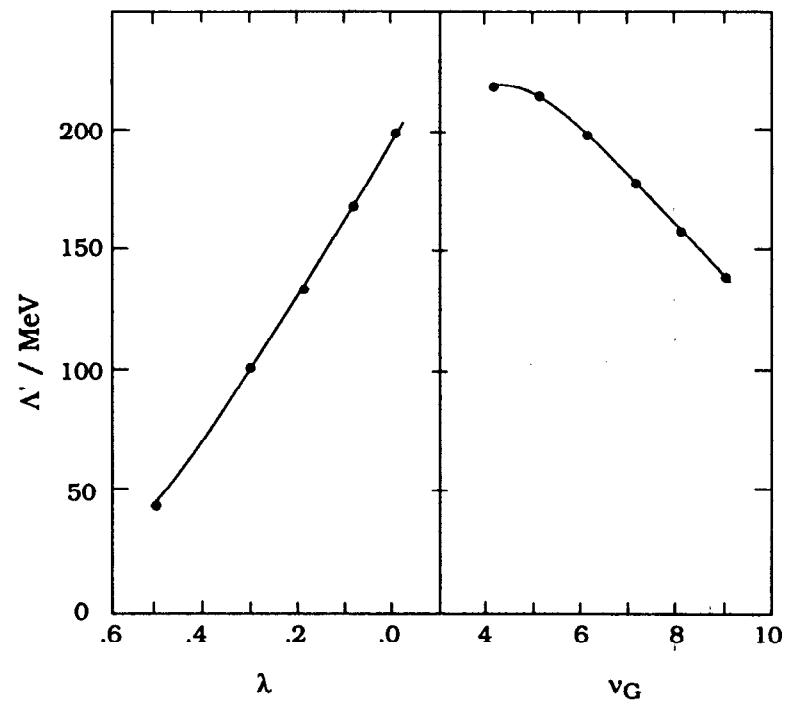


Figure 23: The dependence of Λ on the parameters λ and ν of the input gluon distribution for $x > 0.01$ [36].

x range	type of fit	$\Lambda(\text{MeV})$	α_s	$\langle Q^2 \rangle$
$x \geq 0.25$	NS eq.(4)	175 ± 176	0.132 ± 0.023	2770
$x \geq 0.01$	S,NS eqs.(4,5,6)	177 ± 135	0.159 ± 0.026	400
$x \geq 0.01$	eqs.(4,5,6), $xG(x, Q_0^2)$ fixed	201 ± 25	0.164 ± 0.005	400
$x \geq 10^{-4}$	S,NS eqs.(4,5,6)	225 ± 25	0.204 ± 0.006	80

Table 1: Statistical precision on Λ and α_s from QCD fits to $\hat{\sigma}_{NC}(e^+)$. Warning : the assumed integrated luminosity is 100 pb^{-1} at $x > 10^{-4}$ but reaches 200 pb^{-1} at $x > 0.01$

(for a more detailed comparison see the lecture of T. Hansl-Kozanecka in these proceedings). Alternatively, if we assume that Λ is fixed in the fit, the gluon t , the gluon shape can be determined rather accurately.

Extending the analysis to the smallest x value measurable at HERA would give an unrivalled statistical precision of 2% on Λ or 0.3% on α_s . The evolution at $x < 0.01$ is entirely dominated by the gluon (see Fig. 22). The unfolding of the gluon distribution at very small x is still subject to studies. One analysis has shown [39] that it should be possible to discriminate between a flat gluon and a steep gluon at $10^{-3} < x < 10^{-2}$ in a joint fit of the gluon input distribution and of Λ . The results of this analysis are shown in Fig. 24 for two possible input distributions : the original one of Duke and Owens [40] and a modified distribution where the original has been multiplied by $1/\sqrt{x}$. However, the detailed correlations between the parametrisations of the input gluon shape and the parameter Λ need more investigations. As a last remark, let us remind that the absorption corrections have not been yet included in the fits of the scaling violations. A joint analysis of Λ , of the gluon distribution and of the absorption corrections has still to be worked out.

4.2 Longitudinal Structure Function

From perturbative QCD calculations, the longitudinal structure function $F_L(x, Q^2)$ ($= F_2 - 2xF_1$) or the ratio $R(x, Q^2)$ ($= F_L(x, Q^2)/2xF_1$) are expected to get sizeable contributions at $x < 0.01$ and $Q^2 > 10 \text{ GeV}^2$ but smoothly vanish as $1/\ln(Q^2)$. As illustrated in Fig. 25, spectacular effects are anticipated at HERA energies. We consider hereafter the kinematical domain $Q^2 < 1000 \text{ GeV}^2$, where the Z exchange can be neglected and where R can be related to the polarisation of the virtual photon ($R = \sigma_L/\sigma_T$). We describe first the method of extraction of $xG(x, Q^2)$ from $F_L(x, Q^2)$ and then the usual method to measure F_L (or R) [41]. We complete by a

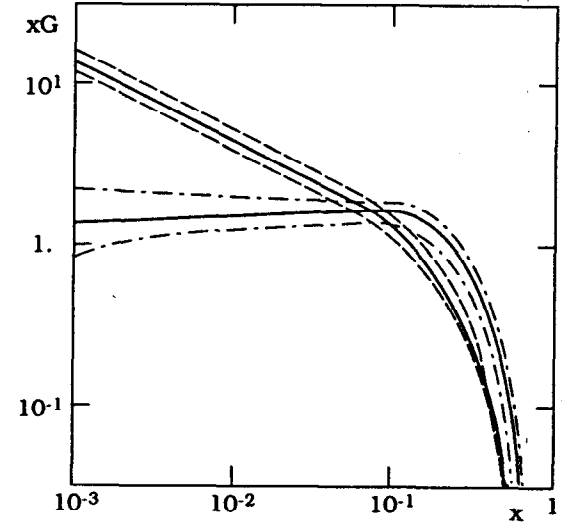


Figure 24: Extraction of the gluon input distribution. $xG \pm \delta xG$ (statistical errors) at $Q_0^2 = 10 \text{ GeV}^2$, from a joint fit to Λ and xG [37]. Dashed-dotted lines : assumed input distribution is xG_{DO} from ref. [38]. Dashed lines : assumed input distribution is $(\frac{0.30}{\sqrt{x}}) xG_{DO}$.

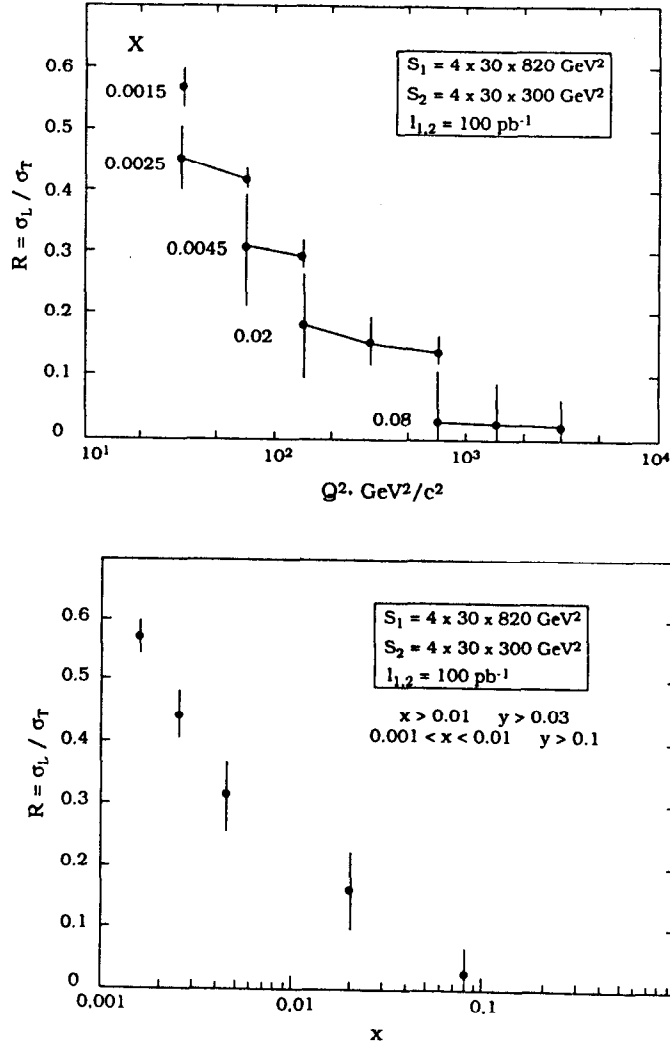


Figure 25: Monte Carlo estimates on $R(x, Q^2)$.
a) R versus Q^2 . At each Q^2 bin, two x intervals are shown.
b) R versus x . At each x bin, R is averaged over the y range, $y > 0.03$ at $x > 0.01$, and $y > 0.1$ at $0.001 < x < 0.01$.

brief presentation on a rather speculative method which has been proposed recently [42].

4.2.1 Method of extraction of $xG(x, Q^2)$ from $F_L(x, Q^2)$

At order $O(\alpha_s)$ and with no shadowing corrections, the QCD predictions for F_L are [43]:

$$F_L(x, Q^2) = \frac{\alpha_s(Q^2)}{4\pi} \left[\frac{16}{3} I_F + 8 \sum_{i=1}^{n_f} e_i^2 I_G \right] \quad (55)$$

where e_i is the quark charge of flavour i and where

$$I_F = \int_x^1 \frac{dy}{y} \left(\frac{x}{y} \right)^2 F_2(x, Q^2) \quad (56)$$

$$I_G = \int_x^1 \frac{dy}{y} \left(\frac{x}{y} \right)^2 \left(1 - \frac{x}{y} \right) yG(y, Q^2) \quad (57)$$

At small x , the integral I_G over the gluon distribution dominates the integral I_F over the quark distribution, so that the measurement of F_L gives an almost direct estimate of the gluon distribution. This is illustrated in Fig. 26 where F_L has been estimated for flat and steep gluon distributions. For an easy unfolding it has been noted [41] that I_F and I_G can be approximated by :

$$I_F(x, Q^2) \sim \frac{1}{2} F_2(2x, Q^2) \quad (58)$$

$$I_G(x, Q^2) \sim \frac{1}{5.9} xG(2.5x, Q^2) \quad (59)$$

and that the approximation is independent of the exact shape of the gluon distribution as $x \rightarrow 0$. The fine tuning of this approximation will be done on the data by iteration. However the basic relation between F_L and the gluon distribution deserves a few theoretical comments :

- The equation (55) has been established at order $O(\alpha_s)$ [43]. Recently $O(\alpha_s^2)$ calculations have been published [44]. Large effects have been found at $x \sim 0.1$ but decreasing when $x \rightarrow 0$. Within the measurement domain at HERA, the contribution of $O(\alpha_s^2)$ terms are at most of 7%, depending on the shape of the gluon [45]. The Higher Order terms can therefore be neglected or used as a small correction.
- In equation (55) the sum runs over all flavours. In the kinematical domain of the fixed targets experiments, the contribution of the b quark can be safely neglected. At HERA the b quark should be included and the sum should run over all five quark flavours. However quark

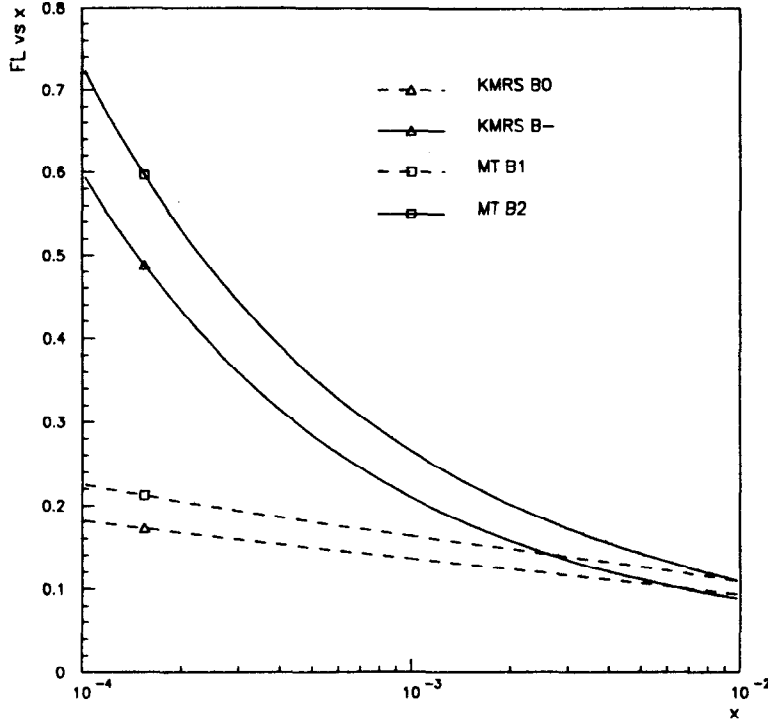


Figure 26: $F_L(x, Q^2)$ at $Q^2 = 10 \text{ GeV}^2$ for various set of parametrisations : KMRS [22], MT [24] and DO [38].

mass effects damp this contribution when the Q^2 value crosses the nominal threshold $Q^2 = 4m_b^2 x/(1-x)$. Mass effects in the gluon term are very small and, as for the $O(\alpha_s^2)$ terms, could be incorporated as a small correction [45].

- We do not know yet how F_L will be modified by the absorption corrections that we have discussed in section 2. Some estimates are being done and should be reported at the 1991 HERA workshop [1].

4.2.2 Measurement of $F_L(x, Q^2)$ by the usual method

In the domain where the contribution of $x F_3$ is negligible, the differential cross section (eq. 41) can be rewritten as :

$$\frac{d^2\sigma}{dx dQ^2} = \frac{4\pi\alpha^2}{xQ^4} \left[\left(1-y + \frac{y^2}{2}\right) F_2(x, Q^2) - \frac{y^2}{2} F_L(x, Q^2) \right] \quad (60)$$

where $x F_1$ has been expressed in terms of F_2 and F_L . It may be also convenient to recast the differential cross section as :

$$\frac{d^2\sigma}{dx dQ^2} = \Gamma \left[\sigma_T(x, Q^2) + \epsilon(y) \sigma_L(x, Q^2) \right] \quad (61)$$

where ϵ is the polarisation of the exchanged virtual photon,

$$\epsilon(y) \sim \frac{2(1-y)}{1 + (1-y)^2} \quad (62)$$

and Γ is the flux of virtual photons,

$$\Gamma = \frac{\alpha}{\pi} \frac{y^2}{2xQ^2} \frac{1}{1 - \epsilon(y)} \quad (63)$$

σ_L and σ_T are the cross sections of longitudinal and transverse-polarised virtual photon respectively (note that for a real photon σ_L is zero). The polarised cross sections are related to F_L and F_2 by,

$$F_L = \frac{Q^2}{4\pi^2\alpha} \sigma_L \quad (64)$$

$$F_2 = \frac{Q^2}{4\pi^2\alpha} (\sigma_L + \sigma_T) \quad (65)$$

It is also convenient to introduce Σ , the relative cross section

$$\Sigma = \Gamma^{-1} \frac{d^2\sigma}{dx dQ^2} = \sigma_T(x, Q^2) + \epsilon(y) \sigma_L(x, Q^2) \quad (66)$$

For a chosen (x, Q^2) it is thus possible to get σ_L and σ_T by measuring the slope and the intercept of Σ versus ϵ . Since ϵ is a function of y and since

$y = Q^2/(4E_e E_p x)$ (eq. 3), the obvious method to have access to various ϵ values is to run at various beam energies.

To illustrate the methods three proton beam energies have been considered (250, 500 and 1000 GeV) which should give a range in ϵ large enough while keeping the electron beam energy to 30 GeV. The predicted behaviour of Σ versus ϵ is shown in Fig. 27a assuming Duke and Owens quark distributions [40] but for two gluon distributions :

$$(A) \quad xG(x, Q^2) = 0.676 \frac{1}{\sqrt{x}} (1-x)^5 \quad (67)$$

$$(B) \quad xG(x, Q^2) = 5(1-x)^5 \quad (68)$$

We note that even for a rather flat gluon distribution, the slope of Σ versus ϵ is measurable. The gluon distribution can be unfolded using equations (55) and (58). The results are shown in Fig. 27b. The measurements are accurate enough to distinguish between the different predictions for the gluon distribution.

It may be pointed out that it is not rigorous to mix quark distributions obtained from a certain gluon shape, with other gluon distributions. This was the only possibility at the time of this study (1987). Since then, more consistent analyses have been made which uphold the real power to get the gluon shape at HERA from the measurements of the longitudinal distribution [1].

4.2.3 Measurement of $F_L(x, Q^2)$ from radiative events

There is another way to vary the energy in the centre of mass rather than changing beam energies. The emission of hard photons of energy E_γ collinear to the electron beam direction leads to a reduction of the effective electron energy which can be measured [42] :

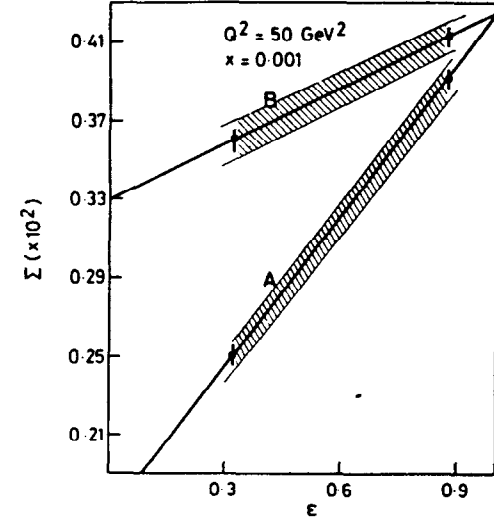
$$E_{eff} = E_e - E_\gamma \quad (69)$$

At very small x , for a chosen (Q^2, x) , varying the energy of the hard photon gives access to a wide range of effective y_{eff} ,

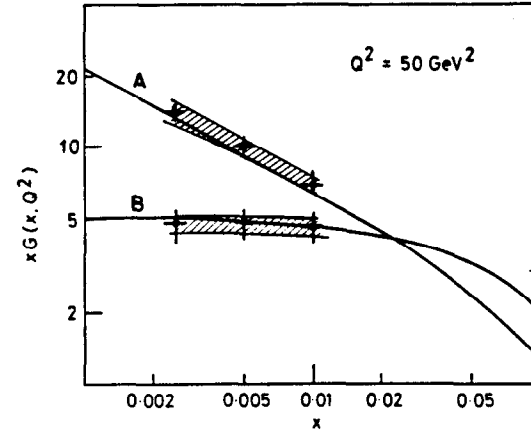
$$y_{eff} = 1 - \frac{E'_e}{E_{eff}} \sin^2(\theta_e/2) \quad (70)$$

and hence to ϵ (eq. 62). This is illustrated in Fig. 28 at $Q^2 = 22.5 \text{ GeV}^2$. The differential cross section for the deep inelastic process $ep \rightarrow e\gamma X$ reads

$$\frac{d^3\sigma}{dx dQ^2 dz} = \alpha^3 P(z) \frac{1 + (1 - Q^2/xzS)^2}{xQ^4} [F_2(x, Q^2) - (1 - \epsilon)F_L(x, Q^2)] \quad (71)$$



a)



b)

Figure 27: (a) Σ measurement versus ϵ at $Q^2 = 50 \text{ GeV}^2$ assuming (A) and (B) gluon shapes from equations (67). The error bars indicate the size of the statistical errors expected for 100 pb^{-1} luminosity at each beam setting. The shaded band indicates the size of the systematic error due to finite resolution and overall normalisation. [39].
(b) Gluon distribution extracted from Σ measurement illustrated in the above Figure a).

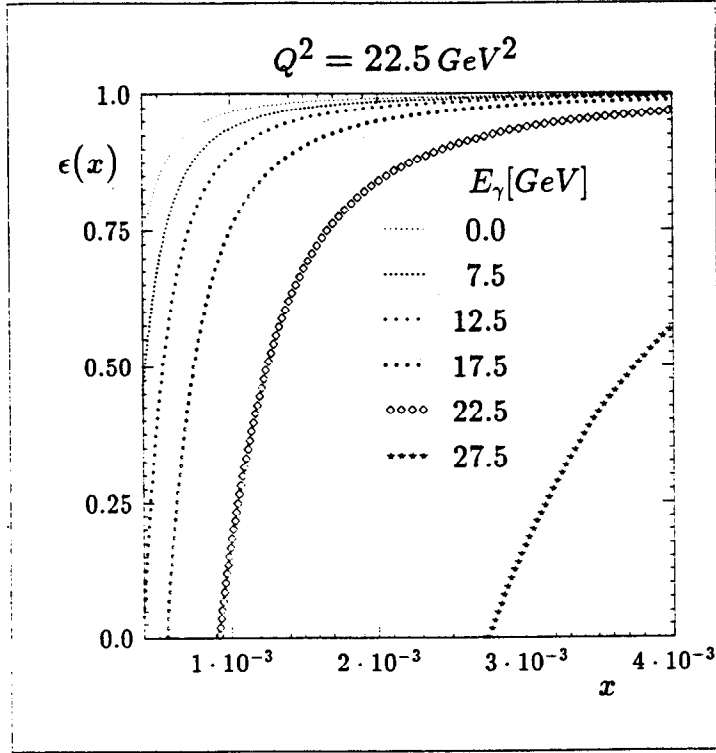


Figure 28: Dependence of ϵ on x for various photon energies with fixed $Q^2 = 22.5 \text{ GeV}^2$.

where

$$z = \frac{E_e - E_\gamma}{E_e} \quad (72)$$

and

$$P(z) = \frac{1+z^2}{1-z} \ln \frac{E_e^2 \theta_M^2}{m_e^2} - \frac{z}{1-z} \quad (73)$$

where θ_M is the largest angle to the electron beam direction at which the hard photon can be detected in the luminosity counters of H1 or ZEUS, the two large HERA detectors. As an example, the photon spectrum of the events in the cell $15 \text{ GeV}^2 \leq Q^2 \leq 30 \text{ GeV}^2$, $0.6 \cdot 10^{-3} \leq x \leq 1.2 \cdot 10^{-3}$ is shown in Fig. 29. We can see that in more than 15% of events, the energy of the emitted photon is larger than 7.5 GeV, thus giving access to a large y range $\Delta y > 0.5$ at a chosen (Q^2, x) .

Similarly to the standard method, the cross section can be recast as

$$\frac{d^3\sigma}{dx dQ^2 dz} = \Gamma \sigma_T (1 + \epsilon R) \quad (74)$$

where now

$$\Gamma = \frac{\alpha^2}{4\pi^2} P(z) \frac{1 + (1 - Q^2/xzS)^2}{xQ^2}. \quad (75)$$

In the method based on radiative events, R is thus obtained from the slopes of a triple differential cross-section versus ϵ . The results are shown in Fig. 30 for an integrated luminosity of 200 pb^{-1} . The statistical precision of the method is encouraging, although not comfortable. The experimental systematics are being studied and are at present larger than the statistical error. The main systematics is due to the pile up in the gamma detector and will depend on the beam conditions. As a last remark let us point out that the measurement of R or F_L has always been very hard and has led to many controversies in fixed target experiments. So, it will be very valuable to have at HERA two completely different methods to measure F_L .

4.3 Photon-gluon Fusion

An entirely different way to get the gluon distribution relies on the production of heavy quark-antiquark pairs by photon-gluon fusion. The Leading Order production diagram is shown in Fig.31. The cross section reads

$$\sigma(ep \rightarrow Q\bar{Q} X) = \int dx_g G(x_g, \hat{s}) \hat{\sigma}(eg \rightarrow Q\bar{Q}) \quad (76)$$

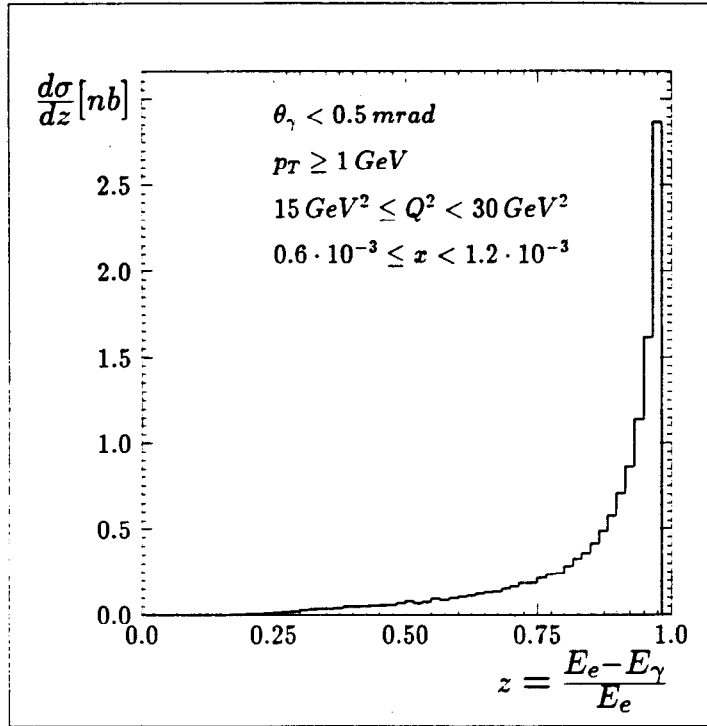


Figure 29: The differential cross section $d\sigma/dz$ for initial state radiation with $\theta_\gamma < 0.5 \text{ mrad}$ integrated over $15 \text{ GeV}^2 \leq Q^2 < 30 \text{ GeV}^2$ and $0.6 \cdot 10^{-3} \leq x \leq 1.2 \cdot 10^{-3}$. Additionally, a cut $p_T \geq 1 \text{ GeV}$ was imposed.

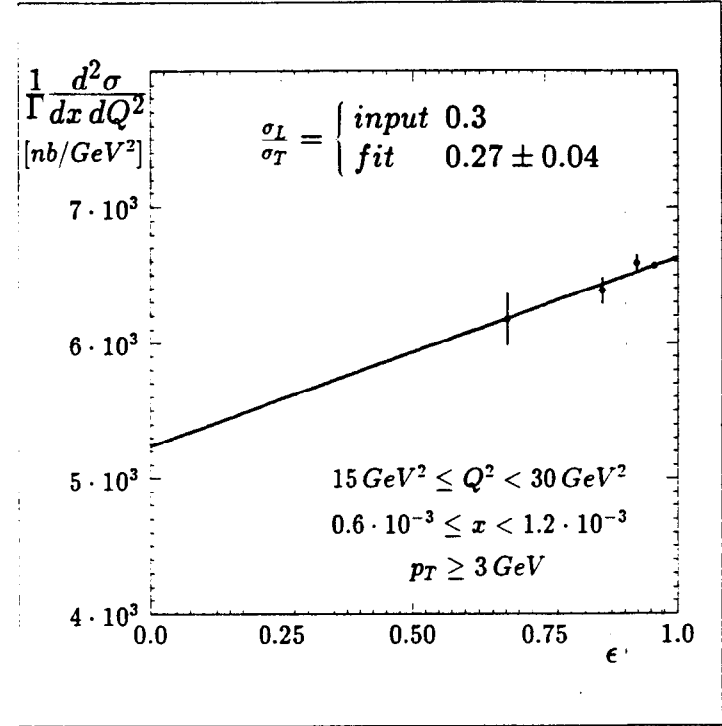


Figure 30: Simulated measurement of $(d^2\sigma/dx dQ^2)/\Gamma$ and a linear fit to the Monte Carlo points for $0.6 \cdot 10^{-3} \leq x \leq 1.2 \cdot 10^{-3}$, $15 \text{ GeV}^2 \leq Q^2 \leq 30 \text{ GeV}^2$, and $p_T \geq 0.1 \text{ GeV}$. Only statistical errors for $\int \mathcal{L} dt = 200 \text{ pb}^{-1}$ are shown.

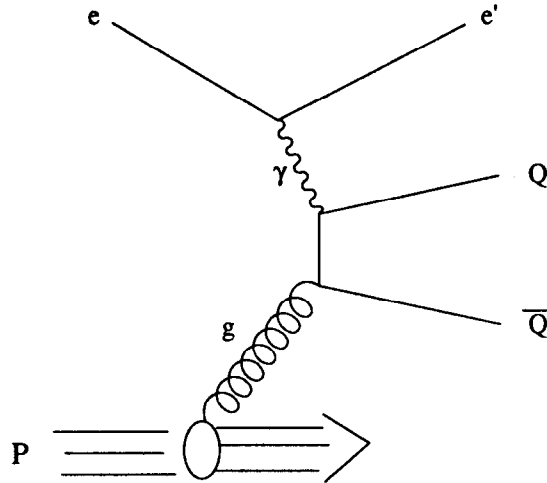


Figure 31: Lowest order QCD diagram for photon-gluon fusion into a heavy quark-antiquark pair.

where $\hat{\sigma}$ is the QCD parton level cross-section and $G(x_g, \hat{s})$ is the probability to find a gluon of momentum $x_g P$ at the mass scale \hat{s} , the invariant squared mass of the $Q\bar{Q}$ system. The momentum fraction x_g of the gluon can be reconstructed from \hat{s} and y :

$$x_g = \frac{\hat{s} + Q^2}{y s} \quad (77)$$

where y can be determined either from the scattered forward electron ($y \sim 1 - E'_e/E_e$) or from the total visible hadron flow (eq. 36). Q^2 is small in photon-gluon processes and can therefore be neglected.

At HERA energies the heavy quark pairs which are easy to identify and produced by photon-gluon fusion at a sufficient rate are the $c\bar{c}$ pairs (500 nb), the inelastic J/Ψ (1.5 nb) and the $b\bar{b}$ pairs (5 nb). So far, only J/Ψ and $c\bar{c}$ events have been studied in detail.

4.3.1 $\gamma g \rightarrow c\bar{c}$

Up to $5 \cdot 10^7$ $c\bar{c}$ pairs will be produced per year at HERA. Several methods have been investigated to tag and reconstruct the $c\bar{c}$ pairs.

Reconstruction from jets When the two jets are produced at high E_T , x_g can be reconstructed from equation (77) where \hat{s} can be approximated [46] by the squared transverse energy $\hat{s} \sim E_T^2$, or by the invariant mass of the two-jets system $\hat{s} \sim M_{jj}^2$.

An alternative method to determine x_g has been proposed recently [47]. It consists of using the rapidity in the laboratory of the two-jets system :

$$\eta_{c\bar{c}} = \frac{1}{2} \ln \left(\frac{y E_e}{E_p x_g} \right) \quad (78)$$

All the three methods give similar resolutions $\Delta x_g/x_g \sim 20\%$, at x_g around 10^{-2} . However, tagging and reconstruction of the $c\bar{c}$ events with jets work only for high transverse energy events ($E_T > 15$ GeV), thus reducing the rate by a factor 500 [46].

Reconstruction from semi-leptonic decays Another way to tag the charmed quarks consists of using the high p_t leptons (muons or electrons). It has been checked that the rapidity of the dilepton system is a good estimate of the rapidity of the $c\bar{c}$ or $b\bar{b}$ system [47,1]. This method is well suited for the analysis of $b\bar{b}$ events where 6000 semi leptonic decays are expected per year (100 pb^{-1}). The expected background contamination is however large and deserves further studies [1].

Reconstruction from D^* tagging A more promising method is to consider the channel

$$c \rightarrow D^{*\pm} \rightarrow D^0 \pi \rightarrow k^\pm \pi^\mp \pi \quad (79)$$

The overall branching ratio is only 1.5 %, but due to the very tight kinematical constraint on the D^* decay, that is $M(D^0 \pi) - M(D^0) \sim 145 \text{ MeV}$, the experimental signature is very clean, as illustrated in Fig.32 [48]. The signal could be still improved by using k/π separation or a secondary vertex detection or flavour separation via neural networks [1].

To reconstruct \hat{s} and hence x_g , there is a simple relation between the transverse momentum p_t of the D^* and \hat{s} :

$$p_t^2 = \hat{s}z(1-z) - M_{D^*}^2. \quad (80)$$

where

$$z = \frac{P_p P_{D^*}}{P_p P_{\gamma^*}} \quad (81)$$

The resolution on x_g is about 40% in the range $5 \cdot 10^{-4} < x_g < 10^{-1}$. A better resolution on x_g (about 25%) could be achieved from the rapidity when the two D^* are reconstructed, but at the expense of a loss of a factor 20 in statistics.

The resulting precision on the gluon distribution from events, where one D^* has been identified, is illustrated in Fig. 33 for a modest integrated luminosity of 6 pb^{-1} and two possible gluon distributions [48]. Open charm events, with D^* tagging, will therefore allow to distinguish between different predictions for the behaviour of the gluon at small x .

As a last point on open charm production, we should mention that there are processes competing with the simple photon-gluon fusion shown in Fig.31. In the so-called resolved photon processes heavy quark pairs are produced by $(q\bar{q} \rightarrow c\bar{c})$ or by $(g\bar{g} \rightarrow c\bar{c})$, where one of the quarks q or one of the gluons g are issued from the virtual photon leg (Fig.34). About 15% of the $c\bar{c}$ pairs are produced by resolved photons [48]. However, the topology of the events should be different for resolved and direct photons. There is some hope that the resolved photon contribution can be eliminated by suitable cuts on the events topology.

We can however remark that, if, on the one hand, resolved photon events are a complication to extract the gluon distribution, they could be, on the other hand, a precious tool to access to the hadronic structure of the photon [50,51]. Furthermore, for well identified direct photon processes there are still some theoretical uncertainties when going from the measured cross section of $Q\bar{Q}$ pairs to the gluon distribution. The equation (76) is only valid in Leading Order. Higher Order terms have been calculated [49]. Large correction factors (K) between 1.5 and 4 are expected at HERA energies.

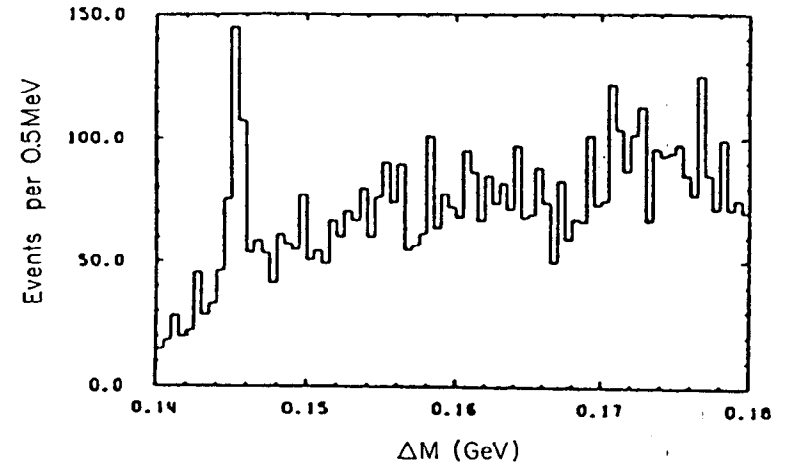


Figure 32: The $\Delta M = M(k^- \pi^+ \pi^-) - M(k^- \pi^+)$ mass difference for $c\bar{c}$ and background events.

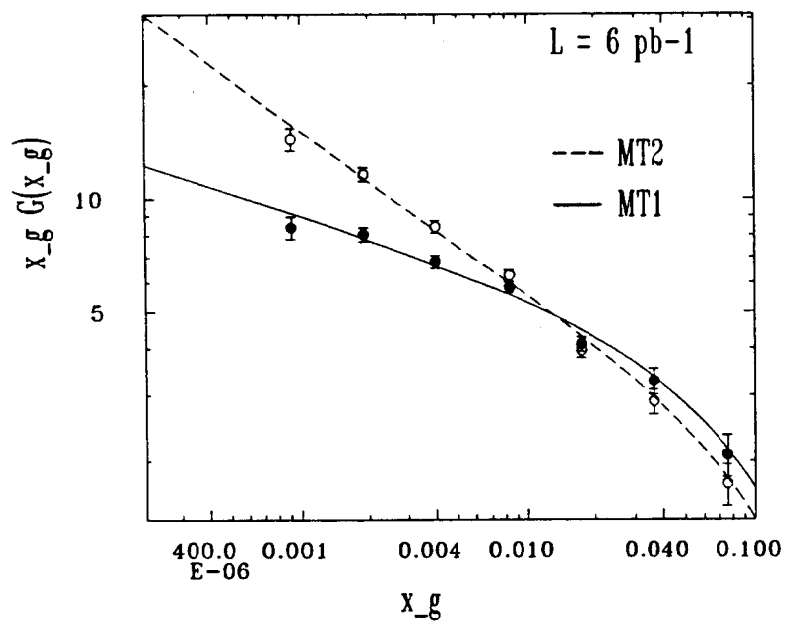


Figure 33: Reconstructed gluon density from D^* production for two sets of parametrizations : Morfin and Tung B_1 and B_2 [24].

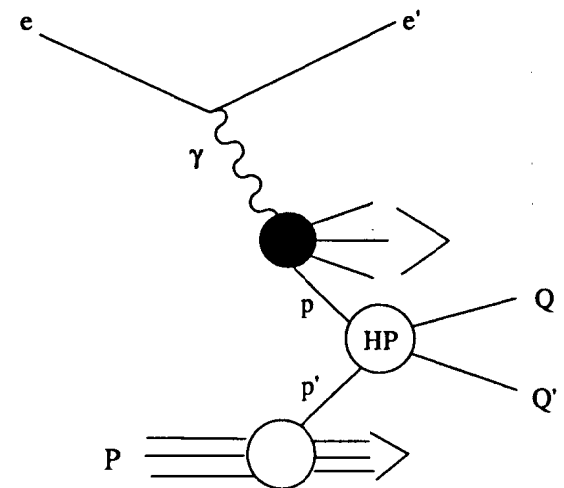


Figure 34: QCD diagram for production of a heavy quark-antiquark pair by resolved photons.

4.3.2 $\gamma g \rightarrow J/\Psi + X$

J/Ψ particles are copiously produced at HERA and relatively easy to identify through their leptonic decay (e^+e^- or $\mu^+\mu^-$). There are however many mechanisms to produce a J/Ψ in ep collisions, that we review in the following before showing how to extract the gluon distribution.

J/Ψ production There are four classes of production processes at HERA energies.

1. The only mechanism relevant to measure the gluon distribution is the inelastic production by direct photons, that is the genuine photon-gluon fusion process. Before any cuts the cross-section production is about 1.5nb . In this process the J/Ψ are produced at some transverse momentum p_t ($> 1\text{ GeV}$) due to a concomitant gluon emission to conserve the colour charge [52] (Fig.35a).
2. The most abundant source of J/Ψ is the diffractive production ($\sigma \sim 36\text{nb}$), that is mainly elastic (Fig.35b). These events are produced at low p_t and large z , where

$$z = \frac{P_p P_{J/\Psi}}{P_p P_\gamma} \quad (82)$$

It is possible to reduce this background to a negligible level by applying the following cuts [1,48] :

$$\begin{aligned} p_t &> 1\text{ GeV} \\ z &< 0.8 \end{aligned} \quad (83)$$

3. J/Ψ can also be produced in decays of B mesons. The estimated cross-section $\sigma \sim 0.09\text{nb}$ is smaller than in the direct photon-gluon process, but B decays become the dominant production mechanism at large p_t ($> 5\text{ GeV}$).
4. The most severe background is coming from the production of J/Ψ by resolved photons, where the J/Ψ (or the χ) is produced by a quark or a gluon from the photon fusing with a quark or a gluon from the proton (Fig.35c). The cross-section is only a factor two smaller than for direct photons. The J/Ψ from resolved photons are however emitted at small angle θ_Ψ with respect to the proton direction and carry a small fraction of the virtual photon energy. Thus requiring

$$\begin{aligned} z &> 0.2 \\ \cos(\Theta_\Psi) &< 0.98 \end{aligned} \quad (84)$$

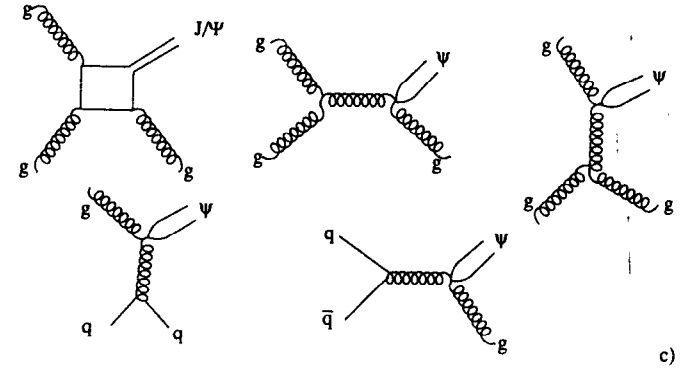
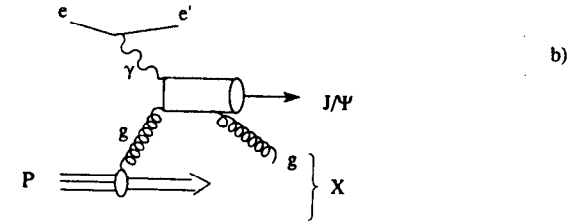
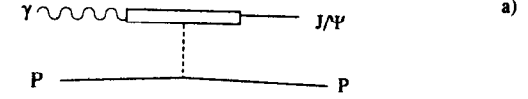


Figure 35: Production diagrams of J/Ψ in ep collisions : (a) diffractive, (b) inelastic from direct photons, (c) resolved photons.

reduces the rate by a factor 10 to 20, while keeping about half of the direct photon events.

In summary, combining the cuts (eq.83 and 84), and taking into account the reconstruction efficiency into the e^+e^- channel, the visible cross-section of J/Ψ production by direct photons is about 40 pb , with a contamination of 10 to 20 % due to resolved photons.

Extraction of the gluon distribution Two completely different methods have been studied to extract the gluon behaviour at small x from J/Ψ events.

1. The first method makes use of a simple expression of the differential cross section in real photoproduction

$$\frac{d\sigma}{dx}(\gamma p \rightarrow J/\Psi X) = xG(x, M_\Psi^2) \frac{\Gamma_{ee}}{M_\Psi^2} f(x, \frac{s_{\gamma p}}{M_\Psi^2}) \quad (85)$$

where f is a known function sharply peaked at a small value x_g , $x_{\text{peak}} \sim C M_\Psi^2/s_{\gamma p}$. C is a constant of order unity and $s_{\gamma p}$ is the squared $\gamma - p$ centre of mass energy. In electroproduction, using the Weizsäcker-Williams Approximation and after integration over the acceptance of the electron tagger in the beam line ($Q_{\min}^2 < Q^2 < Q_{\max}^2$), the differential cross-section reads

$$\frac{d\sigma(e p \rightarrow J/\Psi X)}{dx} = \frac{1.5\alpha}{\pi} \frac{1 + (1-y)^2}{y} \bar{x}G(\bar{x}, M_\Psi^2) \log \frac{Q_{\max}^2}{Q_{\min}^2} \quad (86)$$

where $\bar{x} = 3.4 M_\Psi^2/s_{\gamma p}$. Thus, in order to get the gluon distribution, it is sufficient to identify the inelastic Ψ events in the main detector and to measure y with the electron tagger. This gives very clean results in a x range which is narrow (Fig. 36), but still sufficient to distinguish between the different theoretical predictions on the gluon behaviour at small x [53].

2. In the second method, the momentum fraction x_g of the gluon is determined from \hat{s} and y (eq. 77), like in open charm events. There is a simple relation, similar to equation (80), between \hat{s} and p_t , the transverse momentum of the J/Ψ in the laboratory frame :

$$p_t^2 = \hat{s}z(1-z) + m_\Psi^2(z-1) \quad (87)$$

from which \hat{s} can be reconstructed. In this method, the relative energy of the photon y is reconstructed from the hadron flow in the main detector (eq.36). The gluon distribution is unfolded from the data by

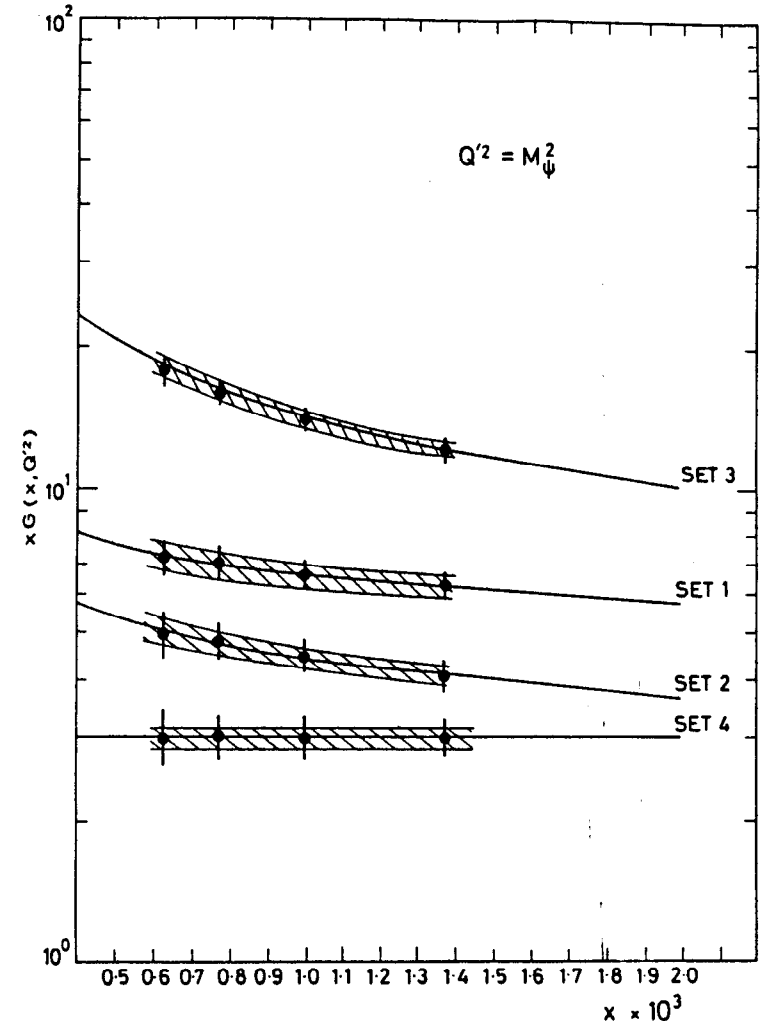


Figure 36: The gluon distributions for four parametrisations superimposed on the measurements of J/Ψ events with the electron tagger [50]. Set 1 is a soft gluon, set 2 is a hard gluon, set 3 the \sqrt{x} gluon and set 4 the $3(1-x)^5$ gluon. The error bars indicate the size of statistical errors expected for an integrated luminosity of 100 pb^{-1} . Shaded bars indicate the size of systematic error due to overall normalisation.

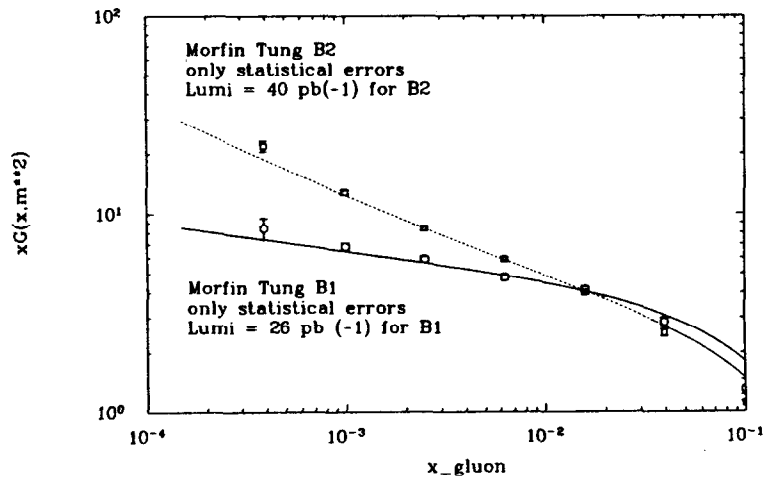


Figure 37: Reconstructed gluon density from J/Ψ production for two sets of parametrisations : Morfin and Tung B_1 and B_2 [24]. The errors are only statistical [51].

Method	x range	Q^2 range(GeV^2)
Scaling violations	$5 \cdot 10^{-4} - 10^{-2}$	10. - 500.
$F_L(x, Q^2)$	$10^{-3} - 10^{-2}$	50. - 500.
$\gamma g \rightarrow J/\psi g$	$4 \cdot 10^{-4} - 10^{-1}$	~ 10 .
$\gamma g \rightarrow c\bar{c}$	$8 \cdot 10^{-4} - 10^{-2}$	~ 100 .

Table 2: Summary on (Q^2, x) domain of measurement of gluon momentum distribution.

fitting the observed $d\sigma/dx$ cross section. Statistically the results [54] are rather encouraging in a large x range, $3 \cdot 10^{-4} < x < 10^{-1}$, as illustrated in Fig. 37. However, we should mention that the theoretical uncertainties are even larger than in open charm events. The K factors do depend on the charmonium model. It is likely that J/Ψ events will only give the shape of the gluon distribution, not the absolute value. This will not affect the power of discrimination between various theoretical predictions on the x behaviour of the gluon distribution (Fig. 37).

4.4 Summary on gluon determination

The (x, Q^2) ranges of the various means to extract the gluon distribution in ep collisions at HERA are summarized in Table 2.

5 More insight into standard physics

In this section we review some complementary aspects to get more insight into the standard model in ep collisions. In addition to the scaling violations and the gluon determination, there are other means to test QCD either in hadronic final states of deep inelastic events or in hard scattering of almost real photon-proton collisions. Moreover, the study of the structure of the proton will not be limited to the new small x domain, the determination of the valence and sea quarks momentum distributions at $x > 0.01$ and very large Q^2 is also one of the primary physics goal at HERA. Finally we should not forget that, especially when the longitudinal polarisation of the electron beam will be well established, some unique electroweak tests will be performed at HERA.

5.1 QCD tests in hadronic final tests

The emission of gluons from the quark lines in the fundamental deep inelastic process $e q \rightarrow e q$ gives rise to a very rich final state. An example of observables which is sensitive to the strong coupling constant α_s is $\Omega(\omega)$ the transverse energy correlation at distance ω [55]. It is defined as :

$$\Omega(\omega) = \frac{1}{N_{event}} \sum_{events} \sum_{i \neq j} \frac{E_{ti} E_{tj}}{Q^2(1-y)} \delta(\omega - \omega_{ij}) \quad (88)$$

with

$$\omega_{ij}^2 = (\eta_i - \eta_j)^2 + (\varphi_i - \varphi_j)^2 \quad (89)$$

where $\eta_i, \varphi_i, E_{ti}$ denote the pseudorapidity, azimuthal angle and transverse energy of particle i in the laboratory frame. The squared transverse momentum of the scattered lepton, $p_{te}^2 = Q^2(1-y)$, is a normalisation factor. As illustrated in Fig.38, the tail at large ω of the $\Omega(\omega)$ distribution could be an order of magnitude above the QPM predictions and thus a very good signature of QCD effects in the hadronic final state. However a precise determination of α_s is plagued by the usual uncertainties between the precise Leading Order Matrix Elements (ME) and the more approximated Parton Shower (PS) calculations at Higher Order where the scale Λ is not defined in a proper renormalisation scheme.

A conceptually more simple determination of the strong coupling constant can be obtained from measuring the relative rates of multijet production. In the Quark Parton Model (QPM), without counting the target remnant jet, one has always one jet in deep inelastic events. In QCD, the ratio of the number of two jets events to the number of one jet events is proportional to α_s in Leading Order. In contrast with the correlation functions, the jets ratios are weakly dependent on the final states modes (PS or ME) [55]. For quantitative estimates, a suitable jet reconstruction algorithm has been tuned to suppress Higher Order multijet events. In this algorithm [56] (LUCIUS in JETSET) particles are joined into clusters as long as their distance d_{ij} is smaller than a given resolution parameter d_{join} , which measures the maximum transverse momentum between particles in a jet. As an example, Fig.39 shows the dependence of the 2 jets over 1 jet ratio on the value of Λ at both the parton level (before fragmentation) and the hadron level [55]. We can see that the statistical errors are very small and that the fragmentation effects play a minor role in the jet ratios. There is however a small difference between the parton and hadron values, which has still to be understood before giving an error estimate on α_s .

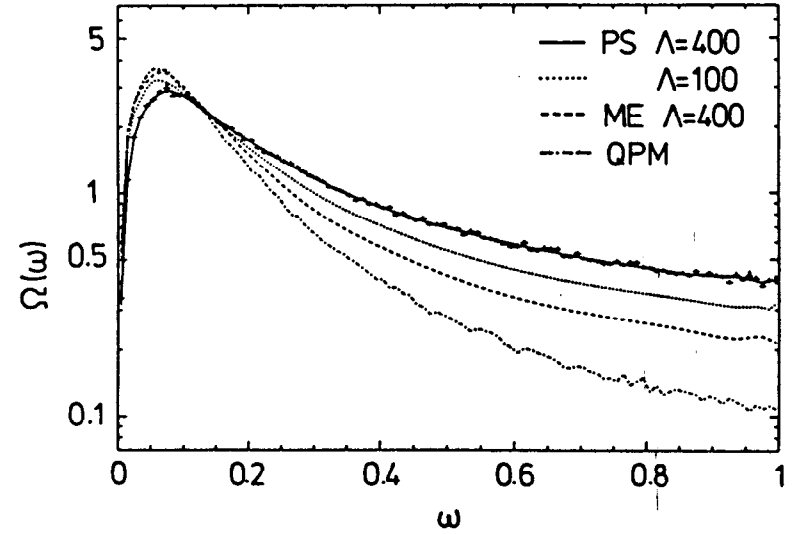


Figure 38: Transverse energy correlation function $\Omega(\omega)$, equation (88). Monte Carlo events with $Q^2, W^2 > 1000 \text{ GeV}^2$ based on the Parton Shower (PS) model, the Matrix Elements (ME) model and the Quark Parton Model (QPM). The error bars correspond to an integrated luminosity of 60 pb^{-1} [52].

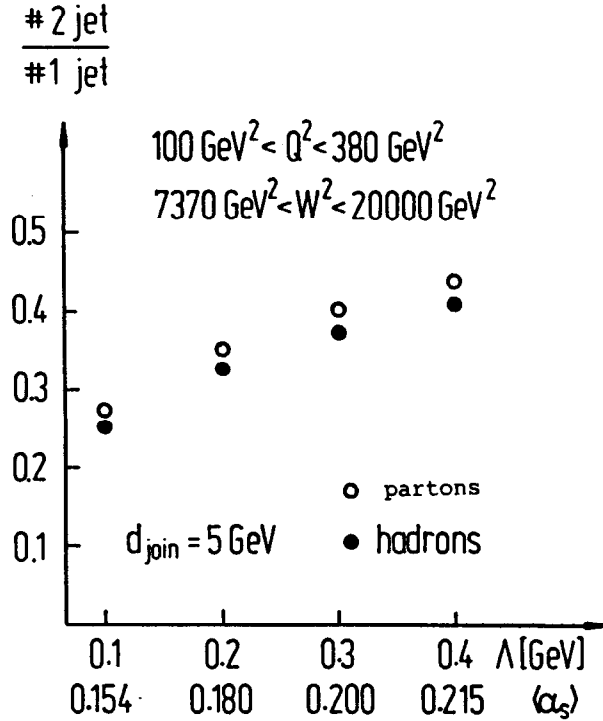


Figure 39: Dependence of the 2-jet / 1-jet ratio (excluding the proton remnant jet) on the Λ parameter [52]. A fixed jet resolution $d_{join} = 5 \text{ GeV}$ has been used. The corresponding mean values of α_s are also given.

5.2 Hard scattering of almost real photons

In most of the interactions at HERA, the scattered electron is emitted at very low angle, the squared transverse momentum Q^2 is almost zero. This gives a unique opportunity to study high energy collisions of almost real photons with protons. A measurement of the total γp cross section is certainly the first experiment to be done. Extrapolating from present data to HERA energies gives an uncertainty of about a factor 10. A more detailed discussion can be found in [1]. As an illustration of the physics potentials, we consider in the following the photoproduction of large transverse momentum jets and the production of prompt photons.

The dominant processes for jet productions are $\gamma q \rightarrow gq$ and $\gamma g \rightarrow q\bar{q}$ where point-like photons (also called direct photons) interact with a quark or a gluon from the proton. There are furthermore other contributions of Higher Order which correspond to quarks or gluons, issued from the quasi real photons, interacting with quarks and gluons from the proton. The Higher Order processes are called resolved photon processes and contribute to the anomalous structure function of the photon. The transverse momentum distribution and the relative importance of the two types of contributions are illustrated in Fig.40 [57]. At large transverse momentum the rates are large and calculable: $5 \cdot 10^4$ jets with $p_t > 10 \text{ GeV}$ per pb^{-1} . A more detailed break down between direct and resolved photons contribution is given in Fig.41 [57]. It is clear that the Higher Order subprocesses (mainly resolved photons) dominate the jet cross section at low and medium p_t . Only at large p_t ($> 50 \text{ GeV}$), the Leading Order (direct photons) dominate. In Fig.40 and 41, the p_t spectrum stops at $p_t > 5 \text{ GeV}$ because at lower p_t there is an other anomalous contribution: the so-called VDM component which should not be neglected. At higher p_t , the hard scattering of almost real photons will be clearly identified and studied for the first time.

Another example of subprocess to test QCD in photoproduction events is the production of real photons at large transverse momentum. As in the photoproduction there are two main sources of contributions:

1. Direct photons:

$$\gamma q \rightarrow \gamma g \quad (90)$$

2. Resolved photons:

$$q^\gamma g^p \rightarrow \gamma q \quad (91)$$

$$g^\gamma q^p \rightarrow \gamma q \quad (92)$$

The corresponding Feynman diagrams are shown in Fig.42. Observation of prompt photons is therefore a source of information on both the proton

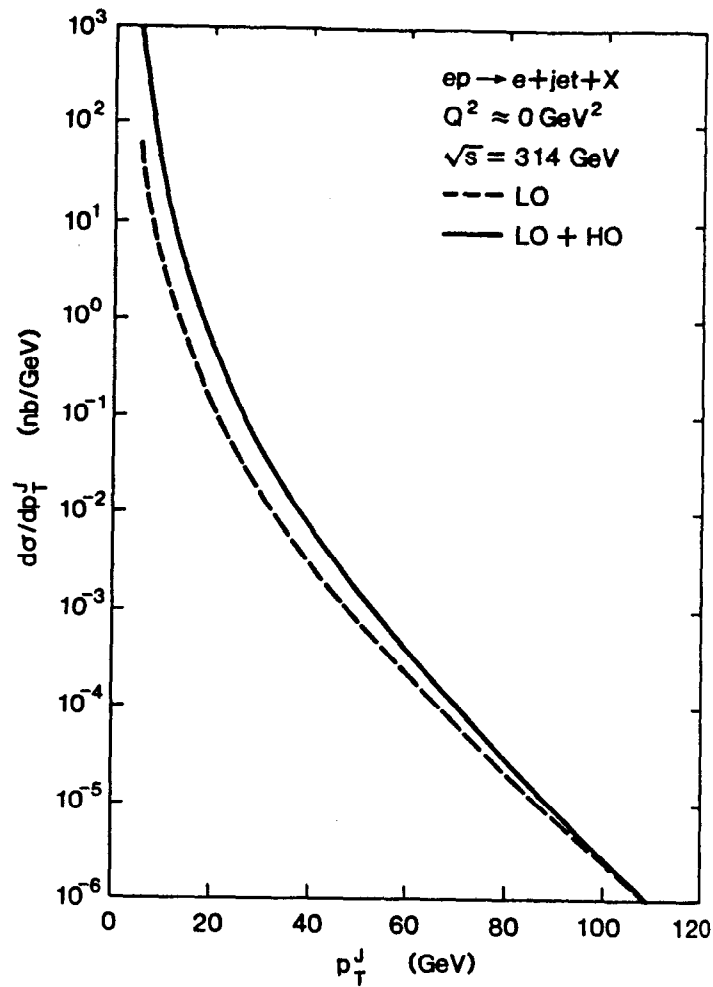


Figure 40: The inclusive jet transverse momentum distribution for $ep \rightarrow e + \text{jet} + X$ [54]. The dashed line is the contribution from the Leading Order processes : $\gamma q \rightarrow gq$ and $\gamma g \rightarrow q\bar{q}$. The solid line includes the Higher Order subprocesses.

Jet p_T distribution : subprocess decomposition

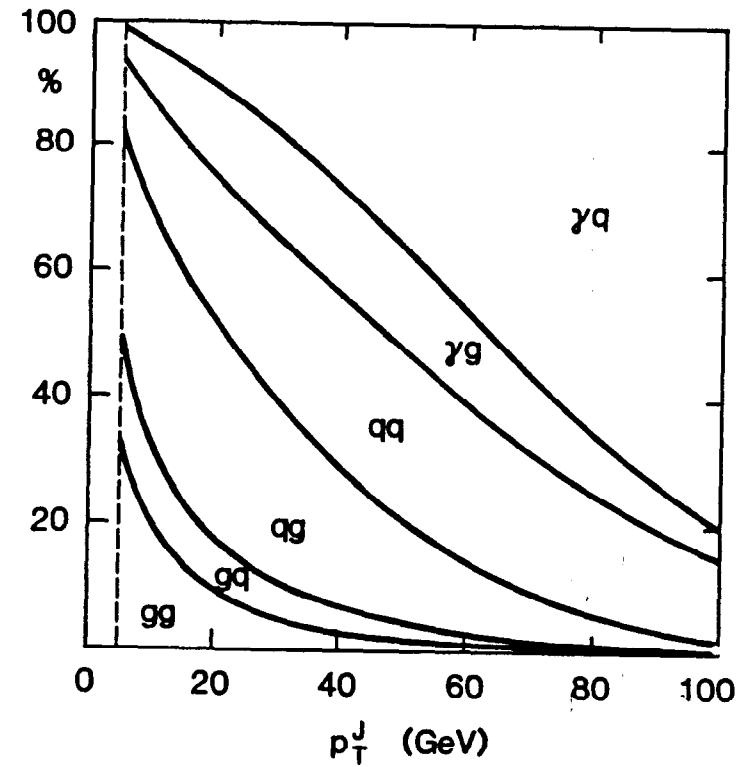
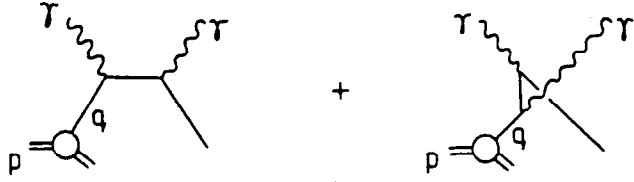
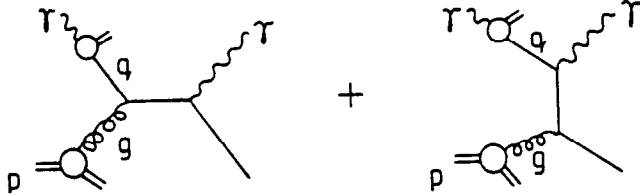


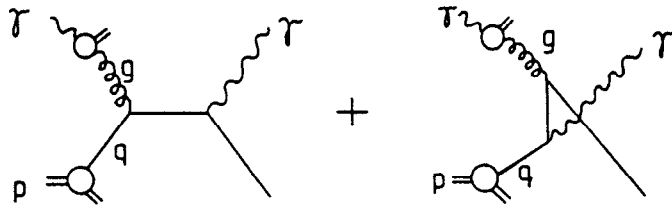
Figure 41: The relative contributions of the different subprocesses to the jet p_T distribution of Fig.40. The first label refers to the constituent of the photon.



The Feynman diagram for the $\gamma^*\gamma \rightarrow \gamma^*\gamma$ Born subprocess.



The Feynman diagram for the $q^*\gamma \rightarrow \gamma q$ subprocess.



The Feynman diagram for the $g^*\gamma \rightarrow \gamma q$ subprocess.

Figure 42: The Feynman diagrams for production of prompt photons .

structure and the anomalous photon structure. As can be seen in Fig.43, the production rates are modest but sufficient. At $p_T^\gamma \sim 20 \text{ GeV}$, we can expect about 40 events per GeV and per year (100 pb^{-1}) [58]. At $p_T^\gamma = 5 \text{ GeV}$, the production cross section by direct photons is two orders of magnitude smaller than by resolved photons. The two modes of production by resolved photons (equations 91 and 92) give rise to different topologies in the laboratory frame. As can be seen in Fig.44, the angular and energy spectrum differ completely [59]. The prompt photons produced by the quark component of the exchanged photons are emitted preferentially at 90° with a low energy. Conversely, all prompt photons produced in the very forward direction (proton side) are very energetic and come from the gluonic component of the exchanged photon. The theoretical predictions are firmly established and do not depend significantly on the assumed parton distributions [58]. Production of prompt photons has been claimed to be a benchmark for standard physics [58], however the experimental aspects and especially the π^0 background deserve very detailed studies.

5.3 Valence and sea quarks momentum distributions

In ep collisions, at HERA energies, it is possible to disentangle (at least partially) the flavour distributions in the differential cross section of not only charged current events (similar to νp collisions) but also of neutral current events thanks to the $x F_3$ contribution (eq. 41 and 42).

Let us consider firstly the charged current events. In the Quark Parton model, when the electron beams are not polarised, the differential cross sections read :

$$\frac{d\sigma_{CC}(e^-)}{dx dy} = \frac{\pi \alpha^2 s}{4 \sin^4 \Theta_W (Q^2 + m_W^2)^2} \left[\sum_{f=u,c} x q_f(x, Q^2) + (1-y)^2 \sum_{f=d,s} x \bar{q}_f(x, Q^2) \right] \quad (93)$$

$$\frac{d\sigma_{CC}(e^+)}{dx dy} = \frac{\pi \alpha^2 s}{4 \sin^4 \Theta_W (Q^2 + m_W^2)^2} \left[\sum_{f=u,c} x \bar{q}_f(x, Q^2) + (1-y)^2 \sum_{f=d,s} x q_f(x, Q^2) \right] \quad (94)$$

It is obvious that at large x ($x > 0.2$), where the sea quark contribution is negligible, the valence quarks can be approximated from :

$$\bar{\sigma}_{CC}(e^+) = (1-y)^2 d_v \quad (95)$$

$$\bar{\sigma}_{CC}(e^-) = u_v \quad (96)$$

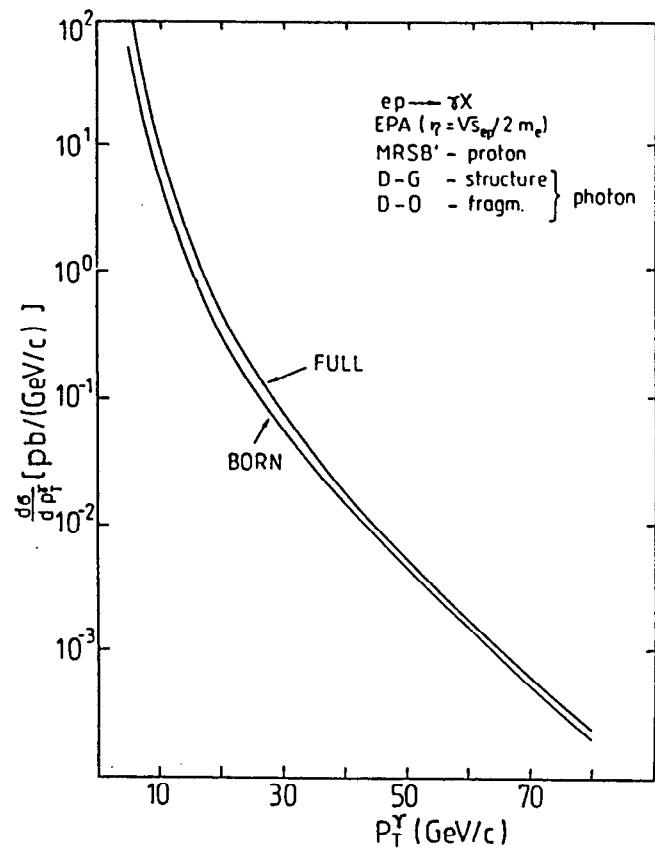


Figure 43: The transverse momentum distribution of prompt photons in the process $e+p \rightarrow \gamma+X$, where the initial state photons are produced assuming the equivalent photon approximation [55]. The curve marked 'FULL' is the cross section with the full set of subprocesses.

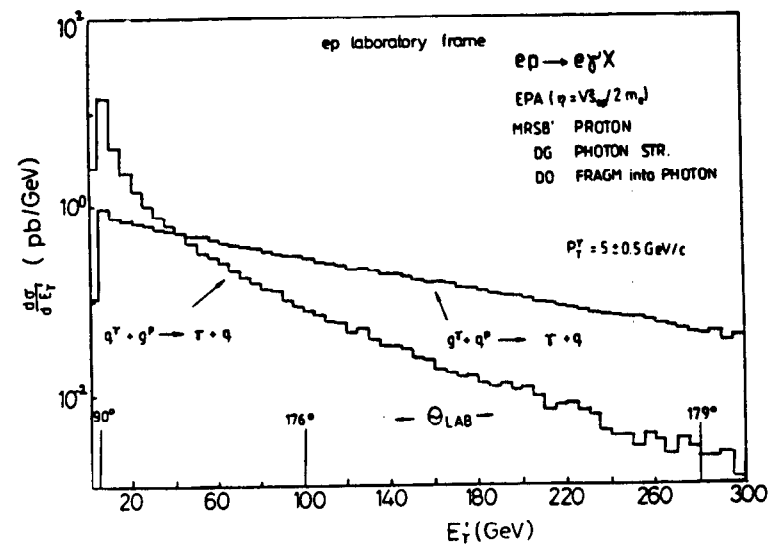


Figure 44: The cross sections $d\sigma/dE_{\gamma'}$ for the prompt photons production due to the resolved photons subprocesses $g^{\gamma}+q^p \rightarrow \gamma+q$ and $q^{\gamma}+g^p \rightarrow \gamma+q$ as a function of the photon energy $E_{\gamma'}$ in the laboratory frame [56]. The corresponding scattering angles are also indicated.

where

$$\bar{\sigma}_{CC}(e^\pm) = \frac{4 \sin^4 \Theta_W (Q^2 + m_W^2)^2}{\pi \alpha^2 s} \frac{d\sigma_{CC}(e^\pm)}{dx dy} \quad (97)$$

The anticipated precision on $\bar{\sigma}_{CC}$, evaluated in the good acceptance domain [60], is given in Fig.45, as a function of x but averaged in Q^2 for an integrated luminosity of 200 pb^{-1} . Also shown are the values of $\bar{\sigma}_{CC}$ at various chosen Q^2 . The average Q^2 at HERA is two orders of magnitude larger than at present fixed target experiments. The shrinking due to the Q^2 evolution should be clearly visible on the up and down valence quarks separately. It should be noted that other quark distributions, for example the pure singlet structure function or $u_v - d_v$, can be obtained by combining CC differential cross sections from e^+ and e^- beams after proper weighting. [60].

As for NC events, in addition to the basic F_2^{em} structure function (see section 4.1, equation 49), the following combination can be extracted :

$$\left(\frac{2}{3}u_v - \frac{1}{3}d_v\right) \sim \frac{\bar{\sigma}_{NC}(e^-) - \bar{\sigma}_{NC}(e^+)}{B_f(Q^2)} \quad (98)$$

where $\bar{\sigma}_{NC}$ and $B_f(Q^2)$ are defined in equations 47 and 44 respectively. The statistical accuracy is rather modest [60].

Much more statistically powerful are the combinations of CC and NC differential cross sections from e^+ and e^- beams. It is possible to exactly unfold quark distributions as :

$$U = u + \bar{u} + c + \bar{c} \quad (99)$$

$$D = d + \bar{d} + s + \bar{s} \quad (100)$$

$$U_{\text{sea}} = U - u_v \quad (101)$$

$$D_{\text{sea}} = D - d_v \quad (102)$$

and many other combinations which can be found in reference [60]. Once the unavoidable systematics when combining data sets with different beam conditions (e^+ and e^-) are well under control, the statistical accuracy on the above quantities should be impressive (Figs.46 and 47) and will drastically improve the knowledge of momentum distributions of valence and sea quarks in free protons.

5.4 Electroweak tests

From the differential cross sections of neutral and charged current events, we have seen that it is possible to extract quark momentum distributions (see section 5.3) and to perform very precise QCD tests (see section 4.1). Moreover, from asymmetries or ratios of cross sections, in which the quark

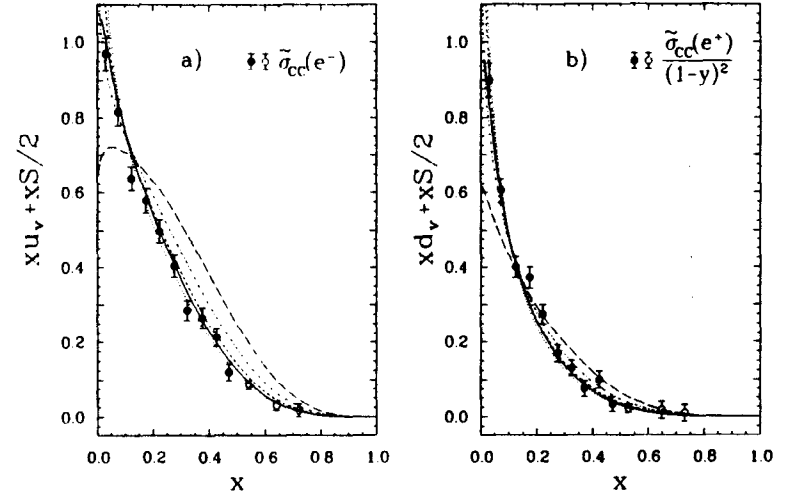


Figure 45: Determination of the quark distributions (a) $x(u_v + S/2)$ from the CC e^- cross section and (b) $x(d_v + S/2)$ from the CC e^+ cross section, averaged over $0.03 < y < 0.15$, where $S = \sum_f (q_f + \bar{q}_f) - u_v - d_v = U_{\text{sea}} + V_{\text{sea}}$ denotes the total quark sea. The Monte Carlo points correspond to an integrated luminosity of 200 pb^{-1} per beam condition [57] and are drawn as full circles in the good acceptance domain (Fig. 20). The curves represent the same quantities evaluated from the input distributions [26] for $Q^2 = 10$ (long-dashed), 10^2 (dash-dotted), 10^3 (dashed), 10^4 dotted GeV^2 and $Q^2 = x y s$ (full).

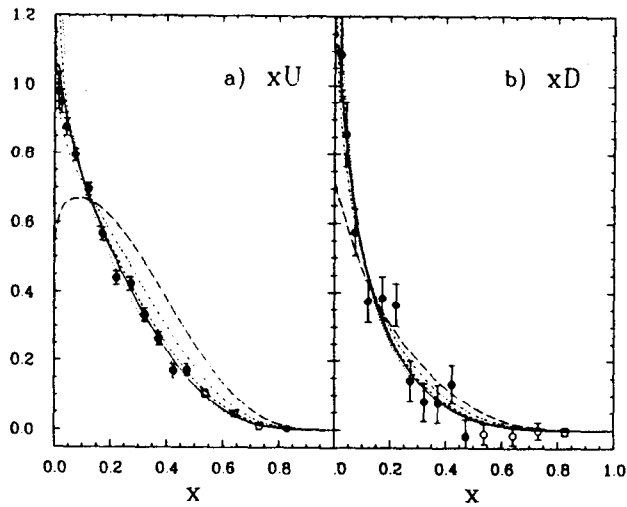


Figure 46: Separate extraction of (a) the total up-type quark distribution $xU = x(u + \bar{u} + c + \bar{c})$ and (b) the total down-type quark distribution $xD = x(d + \bar{d} + s + \bar{s})$ from the NC and the CC e^+p cross sections averaged over $0.03 < y < 0.3$ [57]. Further explanations on the MC result and the curves are given in Fig. 45.

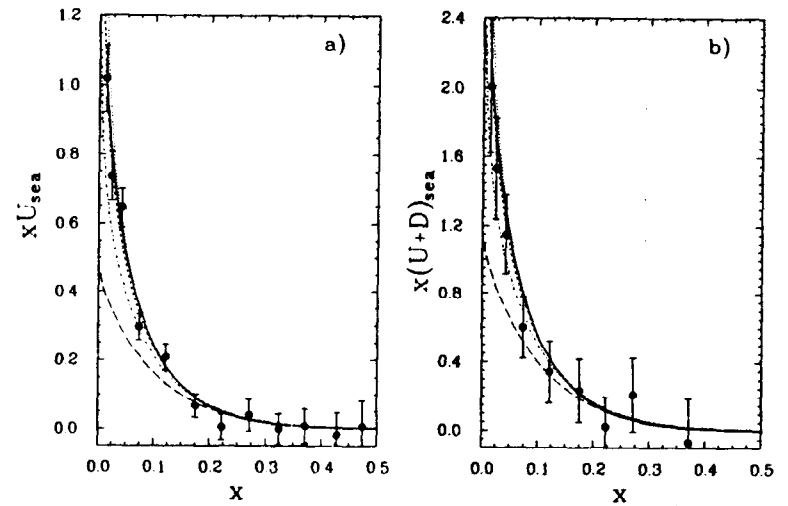


Figure 47: Separate extraction of the sea quark distributions for (a) the up-type quark flavours U_{sea} and (b) all quark flavours $(U_{\text{sea}} + D_{\text{sea}})$ (equ. 99), from the NC and the CC e^+p cross sections, averaged over $0.65 < y < 1$. [57]. Further explanations on the MC result and the curves are given in Fig. 45.

distributions cancel out, it is possible to get electroweak parameters with precisions still competitive at present, but which could be superseded by anticipated results at the FNAL Tevatron or at LEP200. Some of the most efficient tests will be performed with polarised beams. When the electron beams (e^+ or e^-) have a longitudinal polarisation λ the CC cross sections are equal to the unpolarised cross sections (eq.93) multiplied by a factor $(1 - \lambda)$ for e^- beams and a factor $(1 + \lambda)$ for e^+ beams. There are no charged current interactions with e_R^- and e_L^+ 100% polarised beams.

As for the NC cross sections, the coefficients $A_f(Q^2)$ and $B_f(Q^2)$, defined in equation (44), should be modified into [61] :

$$A_f^{L,R}(Q^2) = e_f^2 - 2e_f(v_e \pm a_e)v_f P_Z + (v_e \pm a_e)^2(v_f^2 + a_f^2)P_Z^2 \quad (103)$$

$$B_f^{L,R}(Q^2) = \mp 2e_f(v_e \pm a_e)a_f P_Z + 2(v_e \pm a_e)^2 v_f a_f P_Z^2 \quad (104)$$

In the above relations, the On Mass Shell (OMS) renormalisation scheme has been assumed, that is :

$$m_Z = \frac{m_W}{\cos \Theta_W} \quad (105)$$

Thus, only two of the three parameters are independent. Moreover the mass of the Z^0 is at present so accurately measured, that only one parameter could be improved at HERA, the W mass, m_W . There are many ways to extract m_W from the differential NC and CC cross sections in ep collisions. From detailed studies [62] it turned out that the most precise methods are to consider the ratio of neutral currents to charged current events :

$$R^-(\lambda) = \frac{\sigma_{NC}^-(\lambda)}{\sigma_{CC}^-(\lambda)} \quad (106)$$

or the pure neutral current asymmetry :

$$A^-(-0.8) = \frac{\sigma_{NC}^-(\lambda) - \sigma_{NC}^-(-\lambda)}{\sigma_{NC}^-(\lambda) + \sigma_{NC}^-(-\lambda)} \quad (107)$$

The expected values on R^- and A^- are shown in Fig.48 for an integrated luminosity of 200 pb^{-1} , that is 100 pb^{-1} per beam conditions in the asymmetry measurement and assuming a rather optimistic polarisation of 80%. The resulting precisions on m_W are shown in Fig.49 as a function of the polarisation λ . We can see that the most precise value is obtained from the ratio R^- , and that the precision on m_W depends only weakly on the polarisation of the beam as far as λ is negative or slightly positive (Fig.49). With 80% of polarisation the statistical error on m_W is $\delta m_W = 100 \text{ MeV}$ [62]. The error is only 25% larger when the e^- beam is not polarised. As to the systematic errors, there are two main sources : detector effect and

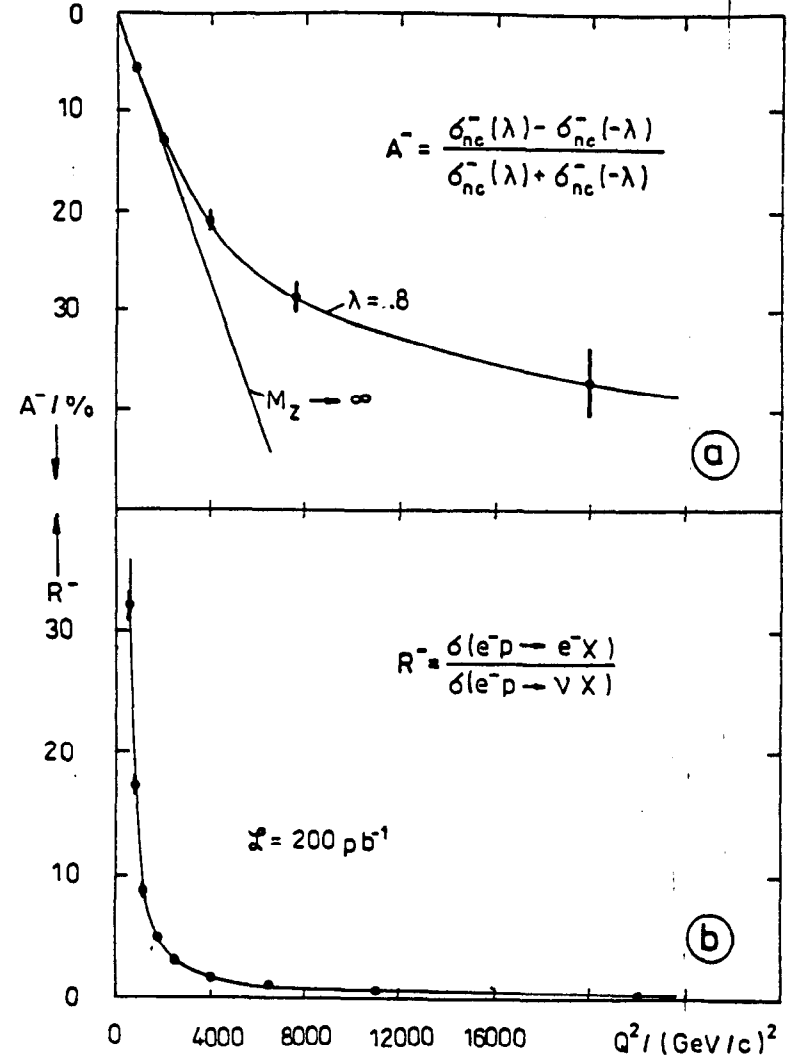


Figure 48: Statistical precision on the neutral current asymmetry A^- and the ratio of neutral to charged current events R^- as a function of Q^2 [59].

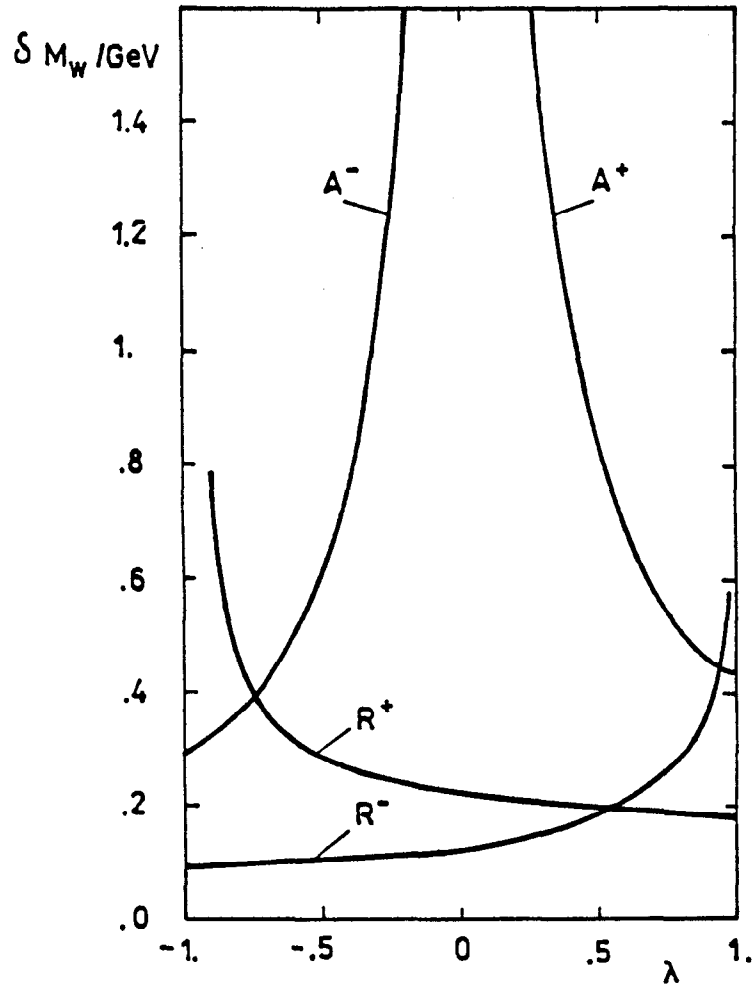


Figure 49: Statistical precision on M_W as a function of the beam polarisations for the pure neutral current asymmetry ratios $A^{+,-}$ and the ratio of neutral to charged current events $R^{+,-}$ [59].

uncertainty on quark momentum distributions. The detector effects are being studied and do not look prohibitive in the ratio R^- [1]. The quark distributions do not cancel out completely in the ratio of neutral current to charged current events. An uncertainty of only 10% on the valence quark u_v or d_v or on the sea quark distributions would induce an error of about 100 MeV on m_W [62].

In summary, when compared to the anticipated precisions on m_W achievable at LEP II or at the FNAL Tevatron, the measurement of electroweak parameters does not look to be the most promising physics at HERA. However, this is only true for precise measurements of electroweak parameters. At HERA, it will be the first time that these parameters will be measured in large space-like Q^2 interactions, moreover the most interesting electroweak physics will be most likely the sensitivity (discovery ?) of physics beyond the Standard Model where the polarisation will bring unrivalled information.

6 Exotic physics

HERA, by exploring a new energy domain, has a certain opportunity window to detect signals beyond the Standard Model. There are many processes not yet excluded by the present data which could be discovered at HERA. We cannot review all of them in this lecture but rather concentrate on a few salient examples. More details can be found in references [63,64,1]. The search for new signals can be divided into two parts : either detecting new particles, for example leptoquarks and heavy Majorana neutrinos, or indirect detection of new dynamics, through the appearance of small systematic deviations from the expected Standard Model cross sections. Examples of new dynamics are exchange of new bosons W' and Z' or compositeness of leptons and quarks.

6.1 Leptoquarks and Leptogluons

Leptoquarks, particles with quantum numbers of both leptons and quarks, and leptogluons are ideal exotic candidates for HERA, since they can be produced as s-channel resonances. Leptoquarks arise in a number of theoretical scenarios (composite models, GUT theories, superstring inspired models) [65,66]. However, only in theories with conserved baryon and lepton numbers, leptoquark masses can be of order 100 GeV [65] :

$$m_{LQ} > g_L 1.7 \text{ TeV} \quad (108)$$

where g_L is the relative coupling constant, defined as the ratio of the coupling constant λ_L^2 to the electromagnetic coupling constant α_{em} , and where

the subscript L denotes the helicity of the coupling and

$$g_L = \frac{1}{4\pi} \frac{\lambda_L^2}{\alpha_{em}} \quad (109)$$

When $g_L = 1$, the coupling is just equal to the electromagnetic coupling. The present experimental limits are of order 100 GeV , well below the kinematical limits at HERA [67]. Production and decay diagrams of leptquarks are shown in Fig.50. A model independent formulation of the cross section reads [65] :

$$\frac{d\sigma}{dx dQ^2}(e_{L,R}^\pm) = \frac{1}{16\pi^2 x^2 s^2} \sum_f \left\{ |A_\gamma + A_Z|^2_{L,R} + 2 \text{Re} [(A_\gamma + A_Z) A_{LQ}^*]_{L,R} + |A_{LQ}|^2_{L,R} \right\} q_f(x, Q^2) \quad (110)$$

where the usual deep inelastic cross section has been recast in terms of the amplitudes A_γ and A_Z multiplied by the quark densities q_f . The leptquark production amplitude A_{LQ} has a simple Breit-Wigner form given by :

$$|A_{LQ}|^2_{L,R} = \frac{1}{2} \frac{\lambda_{L,R}^2 (\lambda_L^2 + \lambda_R^2) \hat{s}^2}{(\hat{s} - m_{LQ}^2) + m_{LQ}^2 \Gamma_{LQ}^2} \quad (111)$$

where $\hat{s} = x s$. The width of the leptquark, Γ_{LQ} , is very narrow ,

$$\Gamma_{LQ} = \frac{1}{16\pi} (2\lambda_L^2 + \lambda_R^2) m_{LQ} \quad (112)$$

thus giving rise to a δ -function like peak in the x distribution at $x = m_{LQ}^2/Q/s$. For a leptquark S , depending on the decay mode (Fig.50), x can be reconstructed either from the scattered electron ($S \rightarrow eu$) or from the hadron flow ($S \rightarrow \nu d$). As is shown in Fig.51 from reference [68], in both methods of reconstruction, the resonance signals in the x distribution are clean, even for couplings as small as $g_L \sim 0.01$. The event rates, for an integrated luminosity of 200 pb^{-1} , are shown in Fig.52. They do depend strongly on the masses and the couplings. A leptquark of mass up to 200 GeV can be discovered at HERA if the coupling value g_L is of order 0.03.

Leptogluons are more speculative, since they couple in a non renormalizable way to leptons and gluons [64]. The production diagram is shown in Fig.53. The amplitude does not interfere with the deep inelastic amplitude, the production cross section is simply given by [69] :

$$\sigma = \frac{8\pi^2 \alpha_s}{s} \frac{m_{LG}^2}{\Lambda^2} G \left(\frac{m_{LG}^2}{s} \right) \quad (113)$$

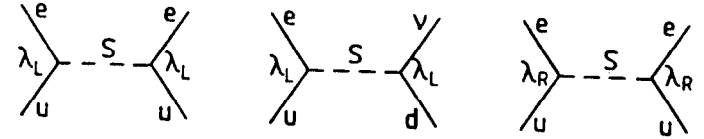


Figure 50: Diagrams for S leptquark production. Note that leptquarks can decay into $S \rightarrow \nu d$, only when the left handed coupling λ is non zero.

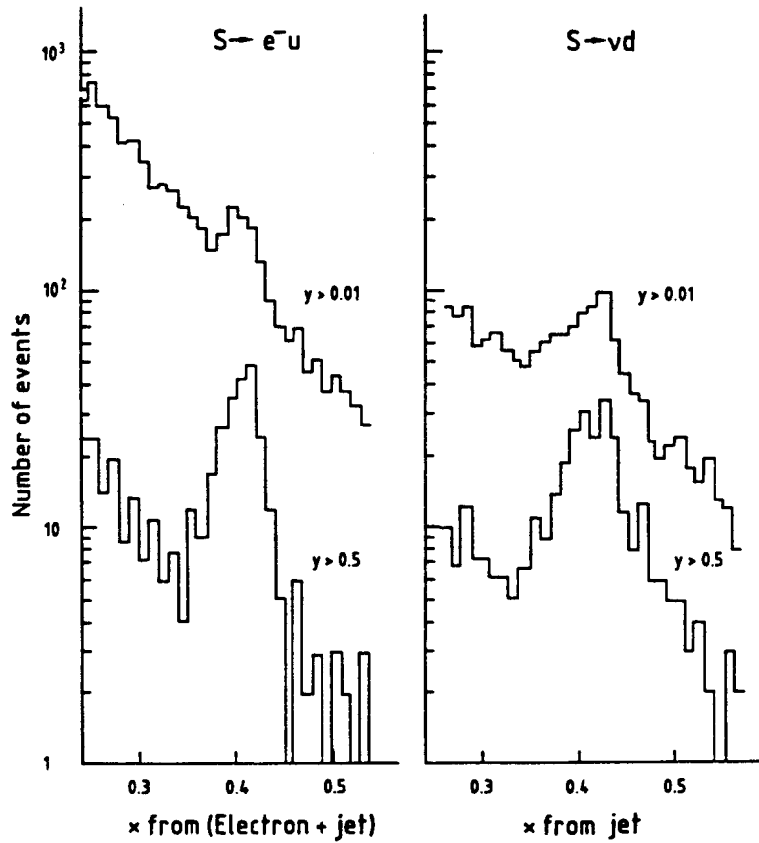


Figure 51: The reconstructed x distribution for the decay of a 200 GeV leptoquark S with couplings $g_L = 0.01$, $g_R = 0$. [65]. The integrated luminosity is 200 pb^{-1} . (a) $S \rightarrow eu$ and (b) $S \rightarrow \nu d$.

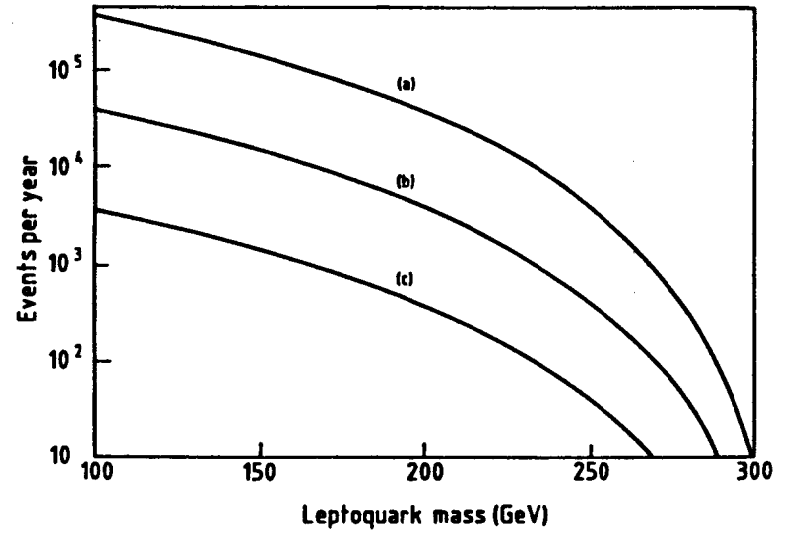


Figure 52: Event rates, for an integrated luminosity of 200 pb^{-1} , as a function of the leptoquark mass, (a) $g_L = 1.0$ (em coupling) and (b) $g_L = 0.1$ and (c) $g_L = 0.01$ [65].

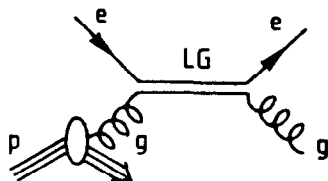


Figure 53: Diagram for leptogluon LG production.

where m_{LQ} is the mass of the leptogluon, Λ the coupling strength and $G(x)$ the gluon density in the proton. The experimental signature should be similar to those of the leptoquarks. But leptogluons have a spin $1/2$, whereas leptoquarks are preferentially scalar particles. It is thus possible to distinguish between leptoquarks and leptogluons by studying the lepton decay angular distributions [68]. Production rates, as shown in Fig.54, depend on the ratio m_{LG}/Λ . In the most favorable case, where $m_{LG} = \Lambda$ [68], leptogluons of mass up to 300 GeV could be discovered at HERA.

6.2 Heavy Majorana neutrinos

Majorana neutrinos are an other example of ideal, but highly speculative, particles which could be directly produced at HERA. In classical theory, lepton number conservation is only sacred when the usual neutrinos (ν_e, ν_μ, ν_τ) are exactly massless. In a number of unified theories, the usual neutrinos get a very small mass and right-handed Majorana neutrinos are added to the fermions of the Standard Model. The mass of the Majorana neutrino reflects the spontaneous breaking of $B - L$, the difference of baryon and lepton number [70]. In ep collisions, Majorana neutrinos can be produced in charged current processes through their mixing with light neutrinos. They could be detected through the decay, $\Delta L = 2$, into a wrong sign electron plus hadrons (Fig.55). Depending on the mixing parameters, but thanks to the very spectacular signature, heavy neutrinos with masses up to 160 GeV can be discovered at HERA nominal beam energies [70].

6.3 New W' and Z' bosons

The existence of additional gauge bosons is predicted by extension of the Standard Model such as compositeness, superstrings, grand-unified theories and Left-Right symmetric. Direct production and detection in some suitable decay channel seems to be out of reach of HERA. The only possibility is to detect some changes in the standard electroweak cross sections due to $Z - Z'$ and $W - W'$ mixing. The sensitivity of HERA to new bosons has been evaluated in the E_6 and Left-Right Symmetric models [71].

6.3.1 W'_R

A W'_R boson which couples to right handed currents is exchanged in the process $ep \rightarrow \nu_R X$. We have seen above that in the specific case where ν_R is a Majorana neutrino of order 100 GeV, spectacular signatures are expected at HERA. But in most of the cases, such as Dirac neutrinos or very heavy Majorana neutrinos, we have to rely on indirect searches. Studies have been made using the Left-Right symmetric model. In this model, a new

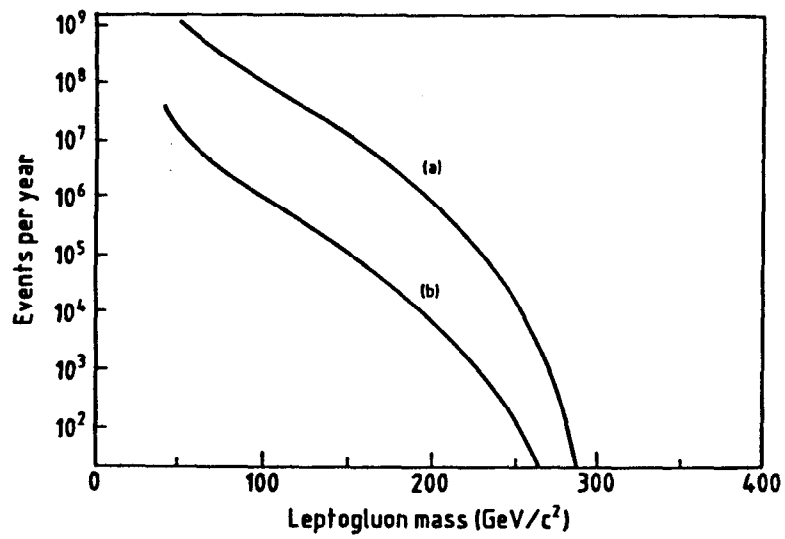


Figure 54: Event rates, for an integrated luminosity of 200 pb^{-1} , as a function of the leptogluon mass, (a) coupling strength $\Lambda = m_{LG}$ and (b) $\Lambda = 10m_{LG}$ [65].

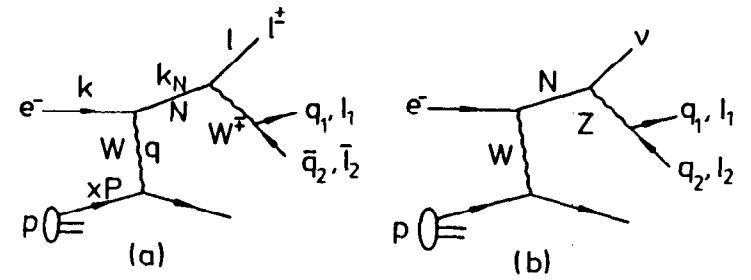


Figure 55: Production and decay of heavy Majorana neutrinos.

group $SU(2)_R$, whose coupling is equal to those of the standard $SU(2)_L$ group, is added. For quantitative estimates an integrated luminosity of 125 pb^{-1} and a polarisation of 80% have been assumed. An upper bound of 400 GeV could be put on $m_{W'_R}$ if no effect is observed in the cross section $d\sigma(e^-)/dQ^2$, at the 90% confidence level [71].

6.3.2 Z'

Studies of sensitivities to a new Z' boson have been made in the same Left-Right symmetric model as in W'_R searches. The most sensitive observable is A_{RR}^+ , the asymmetry between electron and positron polarised righthanded beams. An upper bound of 470 GeV can be reached [71]. However, the sensitivity to a new weak boson depends strongly on the model considered. Another quantitative estimate has been made in the E_6 model. In this model, two $U(1)$'s groups, $U(1)_\chi$ and $U(1)_\psi$, are added to the standard $SU(3)_C \times SU(2)_L \times U(1)_Y$ groups [72]. The Z' boson is a superposition of the $U(1)_\chi$ and $U(1)_\psi$ gauge fields Z_ψ and Z_χ , respectively :

$$Z' = Z_\psi \cos \alpha + Z_\chi \sin \alpha \quad (114)$$

The upper bounds on the Z' mass which can be reached at HERA vary by a factor 3 as a function of the mixing angle α [71]. The highest bound in E_6 models amounts to 300 GeV and is obtained when $\sin \alpha = 1$ (i.e. $\cos \alpha = 0$). In this specific case the best observable is the unpolarised cross section $d\sigma(e^+)/dQ^2$.

6.4 Contact Interactions

New physics at a mass scale Λ of order 1 TeV can be detected in ep collisions at a much lower energy $Q^2 \ll \Lambda^2$, through interference of the γ and Z field with the new neutral current. The effective Lagrangian reads, in an obvious notation :

$$\mathcal{L}^{eff} = \mathcal{L}^{SM} + \mathcal{L}' \quad (115)$$

The exotic Lagrangian \mathcal{L}' has the simple form of a point-like four-fermion Lagrangian when the new physics manifests itself as residual contact interactions at low energy. These interactions could be remnants of a new confining force associated with a further level of substructure (compositeness) and interchange of common subconstituents. However, as indicated in Fig.56, also the exchange of new heavy bosons or new vector boson resonances can lead to similar four-fermion interactions [73]. The most general four-fermion Lagrangian with helicity and flavour conservation reads :

$$\mathcal{L}' = \pm \frac{g^2}{\Lambda^2} (\bar{e} \gamma^\mu e)_a (\bar{q} \gamma_\mu q)_b \quad (116)$$

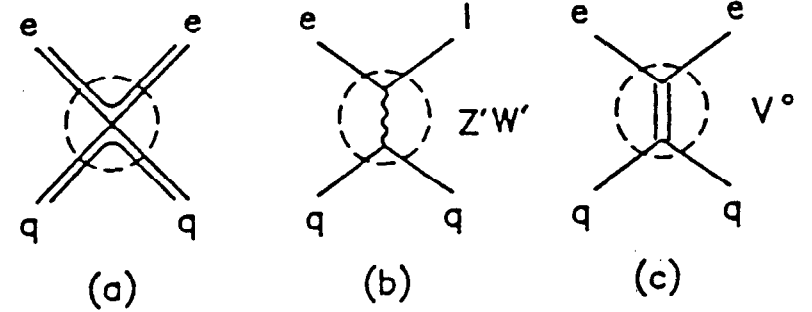


Figure 56: Effective four-fermion interaction generated by (a) interchange of subconstituents, (b) exchange of new heavy gauge bosons, and (c) exchange of heavy vector meson resonance [70].

where the indexes a and b denote the chiral structure of the current (Left, Right, Vector, Axial). It is convenient to define a scale of compositeness Λ^* as :

$$\frac{1}{\Lambda^{*2}} = \frac{1}{4\pi} \frac{g^2}{\Lambda^2} \quad (117)$$

leaving Λ^* as the only free parameter.

To assess the sensitivity to Λ^* , a χ^2 analysis was performed by comparing the Standard Model predictions to the contact interaction on asymmetries between various lepton charges and polarisation states [74]. The resulting sensitivity limits of HERA for the scale of compositeness ranges between 3 and 7 TeV, depending on the chiral structure of the interaction. Without polarisation these limits would be 1 to 2 TeV lower.

7 Conclusion

With HERA it will be possible to explore the proton in a domain two orders of magnitude smaller in x and two orders of magnitude larger in Q^2 than what has been reached in fixed target experiments. With the advent of the first data in spring 1992, the most promising topics for early physics seem to be the deep inelastic scattering at very small x and the hard processes of almost real photon proton collisions. Without, of course, excluding a surprise when, for the first time, an electron and a quark will collide with 314 GeV in the centre of mass. On a longer time scale, the Standard Model will be tested on a number of new facets, with the (secret) hope for experimentalists and theorists that the famous deviations from the Standard Model will be first established at HERA, but may be only with longitudinally polarised beams.

Acknowledgment

I am indebted to M. Besançon, G. Cozzika, A. De Roeck, W. Krasny, J.F. Laporte and C. Royon for a critical reading of the manuscript. I gratefully acknowledge useful discussions with J. Bartels and E. Levin.

References

- [1] Proceedings of the Workshop "Physics at HERA", held at DESY, oct. 1991, to be published
- [2] L.V.Gribov, E.M.Levin and M.G.Ryskin, Nucl. Phys. B188 (1981) 555; Phys. Rep. 100 (1983)
- [3] A.H.Mueller and J.Qiu, Nucl. Phys. B268 (1986) 427
- [4] J.P.Blaizot and A.H.Mueller, Nucl. Phys. B289 (1987) 847
- [5] J.C.Collins, in Proc. 7th Topical Workshop on Proton-Antiproton Collider Physics, Fermilab, 1988
- [6] A.H.Mueller and H.Navelet, Nucl. Phys. B282 (1987) 727
- [7] V.N.Gribov and L.N.Lipatov, Sov.Journ.Nucl.Phys. 15 (1972) 438 and 675
- [8] G.Altarelli and G.Parisi, Nucl.Phys. 126 (1977) 297
- [9] Yu.L.Dokshitzer, Sov.Phys.JETP 46 (1977) 641
- [10] BCDMS coll., A.C. Benvenuti et al., Phys.Lett. B223 (1989) 485; Phys.Lett. B237 (1990) 592
- [11] CCFR coll., S.R.Mishra et al., talk at EP-HEP 91 conference, Geneva, July 1991
- [12] D.J.Gross and F.Wilczek, Phys.Rev. D8 (1973) 3633 and D9(1974) 980; H.Georgi and H.D. Politzer, Phys.Rev. D9 (1974) 416
- [13] E.A.Kuraev, L.N.Lipatov and V.S.Fadin, Phys.Lett. 60B (1975) 50 and Zh.Eksperiment.I.Teor.Fiz. 72 (1977) 377
- [14] J.Kwiecinski, A.D.Martin and P.J.Sutton, preprint DTP/91/10, University of Durham (England)
- [15] Ya.Ya.Balitski and L.N.Lipatov, Sov.J.Nucl.Phys. 28 (1978) 822
- [16] G.Marchesini and B.R.Webber, Nucl.Phys. B349 (1991) 617
- [17] S.Catani, F.Fiorani and G.Marchesini, Phys.Lett. B234 (1990) 339; Nucl.Phys. B336 (1990) 18
- [18] E.M.Levin et al., Nucl.Phys. B357 (1991) 167

- [19] E.Reya, preprint DO-TH 91/09 (Dortmund)
- [20] E.M.Levin, preprint DESY 91-110, talk at EP-HEP 91 Conference, Geneva, July 1991
- [21] J.Bartels, J.Blümlein and G.A.Schuler, Z.Phys. C50 (1991) 91
- [22] J.Kwiecinski A.D.Martin, W.J.Stirling and R.G.Roberts, Phys.Rev. D 42 (1990) 3645
- [23] E.M.Levin and M.G.Ryskin, Frascati Preprint, LNF-90/025(PT)
- [24] J.Morfin and Wu-Ki-Tung, preprint Fermilab-Pub 90/74 (1990)
- [25] M.Glück, E.Reya and A.Vogt, Z.Phys. C48 (1990) 471; preprint DO-TH 91/07
- [26] E.Eichten et al., Rev. Mod. Phys. 56 (1984) 579 and erratum 58 (1986) 1065
- [27] J.Bartels, C.Charchula and J.Feltesse, to be published in Proceedings of the Workshop "Physics at HERA", held at DESY, oct. 1991
- [28] A.H. Mueller, Nucl. Phys. B (Proc. Suppl.) 18C (1990) 125
- [29] J.Bartels et al., 'Measurements of Hot Spots at HERA', to be published in Proceedings of the Workshop "Physics at HERA", held at DESY, oct. 1991
- [30] M.G. Ryskin, Yad. Fiz. 52 (1990) 828 and Nucl. Phys. B (Proc. Suppl.) 18C (1990) 162
- [31] E.M.Levin and M.G.Ryskin, Sov. J. Nucl. Phys. 21 (1975) 206. A.Capella and A. Krzywicki, Phys. Rev.D18 (1978) 4120
- [32] J.Feltesse, Proceedings of the HERA Workshop, Hamburg, october 1987
- [33] J.Blümlein and Max Klein, Zeuthen preprint PHE 90-19 (1990)
- [34] Proceedings of the study of an ep facility for Europe, Ed. U.Amaldi, DESY 79/48 (1979) 391-394
- [35] J.Feltesse, Proceedings of the 1989 International Symposium Lepton and Photon Interactions at High Energies, Stanford University (1989) p.13
- [36] C.G.Callan,D.J.Gross,Phys.Rev.Lett. 22 (1969) 156
- [37] J.Blümlein et al.,Z.Phys. C45 (1990) 501
- [38] J.Blümlein et al., Proceedings of the HERA Workshop, Hamburg, oct. 1987, vol. 1 p.67
- [39] J.Blümlein, M.Klein and Th.Naumann, Zeuthen preprint PHE 88-12 (1988)
- [40] D.W.Duke and J.F.Owens, Phys. Rev. D30 (1984) 49
- [41] A.M.Cooper-Sarkar et al., Z.Phys. C39 (1988) 281
- [42] M.W.Krasny, W.Placzek and H.Spiesberger, Saclay preprint DPHPE 91-11
- [43] G.Altarelli and G.Martinelli, Phys. Lett.76B (1978) 89
- [44] D.I.Kazakov et al., Phys. Rev. Lett. 65 (1990) 1535 and 65 (1990) 2921 (E)
- [45] H.Orr and W.J.Stirling, Phys. Rev. Lett. 66 (1991) 1673
- [46] G.d'Agostini and G.Monaldi, Z.Phys. C48 (1990) 467
- [47] K.J.Abraham et al., CERN 90-10, proceedings of the LHC collider, Aachen, oct. 1990, vol II, p.899
- [48] F.Ould-Saada, in Proc. 4th Symp. on Heavy Quark Physics, Orsay, 25-29 june 1991; H1 Int. Rep. H1-11/91-199
- [49] R.K.Ellis and P.Nason, Nucl.Phys. B312 (1989) 551, S.Catani, M.Ciafaloni and F.Hautmann, Cavendish-HEP-90/27
- [50] R.S. Fletscher et al., MAD/PH/633, BA-91-17 (1991)
- [51] P.Aurenche et al., to be published in Proceedings of the Workshop "Physics at HERA", held at DESY, oct. 1991
- [52] E.L.Berger and D.Jones, Phys.Rev. D23 (1981) 1521
- [53] S.M.Tkaczyk, W.J. Stirling and H.Saxon, Proceedings of the HERA Workshop, Hamburg, oct.1987, Vol. 1 p.165
- [54] H.Jung et al., to be published in Proceedings of the Workshop "Physics at HERA", DESY, oct. 1991
- [55] M.Bengtsson, G.Engelman and B.Naroska, Proceedings of the HERA Workshop, Hamburg, oct.1987, Vol. 1 p.281

- [56] T.Sjöstrand, Computer Phys. Comm. 28 (1983) 229
- [57] W.J.Stirling and Z.Kunszt, Proceedings of the HERA Workshop, Hamburg, oct.1987, Vol. 1 p.331
- [58] A.C.Bawa, M.Krawczyk and W.J.Stirling, Z.Phys. C50 (1991) 293
- [59] A.C.Bawa and M.Krawczyk, Phys. Lett. B 262 (1991) 492
- [60] G. Ingelman and R.Rückl, Z.Phys. C44 (1989) 291
- [61] G.Ingelman et al., Proceedings of the HERA Workshop, Hamburg, oct.1987, Vol. 1 p.3
- [62] J.Blümlein, M.Klein and T.Riemann, Proceedings of the HERA Workshop, Hamburg, oct.1987, Vol. 2 p.687
- [63] R.J.Cashmore et al., Phys.Rep. 122C (1986)277
- [64] R.D.Peccei et al., Proceedings of the HERA Workshop, Hamburg, oct.1987, Vol. 2 p.797
- [65] W.Buchmüller, R.Rückl and D.Wyler, Phys. Lett. 191B (1987) 442
- [66] J.Bijnens, Proceedings of the HERA Workshop, Hamburg, oct.1987, Vol. 2 p.819
- [67] B.Schremp et al., to be published in Proceedings of the Workshop "Physics at HERA", held at DESY, oct. 1991
- [68] N.Harnew, Proceedings of the HERA Workshop, Hamburg, oct.1987, Vol. 2 p.829
- [69] U.Baur and K.H.Streng, Z.Phys. C30 (1986) 325 and K.H.Streng, Z.Phys. C33 (1986) 247
- [70] W.Buchmüller and C.Greub, preprint DESY 91-034
- [71] F.Cornet and R.Rückl, Proceedings of the HERA Workshop, Hamburg, oct.1987, Vol. 2 p.771
- [72] D.London and J.L.Rosner, Phys.Rev.D34 (1986) 1530
- [73] R.Rückl, CERN 90-10, proceedings of the LHC collider, Aachen, oct. 1990, vol I, p.229
- [74] H.U.Martyn, Proceedings of the HERA Workshop, Hamburg, oct.1987, Vol. 2 p.801